

**Modeling tabular icebergs submerged in coupled-to an ocean model**

**A. A. Stern<sup>1</sup>, A. Adcroft<sup>1</sup>, O. Sergienko<sup>1</sup>, G. Marques<sup>1</sup>**

<sup>1</sup>Geophysical Fluid Dynamics Laboratory, Princeton University  
<sup>1</sup>201 Forrestal Rd, Princeton, NJ 08540, USA

**Key Points:**

- A novel modeling framework is developed to explicitly model large tabular icebergs submerged in the ocean.
- Tabular icebergs are represented using Lagrangian elements that drift in the ocean, and are held together by numerical bonds.
- Breaking the numerical bonds allows us to model iceberg breakup and calving.

12 **Abstract**

13 Large tabular icebergs calved from Antarctic ice shelves have long lifetimes (due to their  
 14 large size), during which they drift across large distances, altering ambient ocean circu-  
 15 lation, bottom-water formation, sea-ice formation, and biological primary productivity  
 16 in the icebergs' vicinity. However, despite their importance, the current generation of  
 17 ocean circulation models **usually** do not represent large tabular icebergs. In this study  
 18 we develop a novel framework to model large tabular icebergs submerged in the ocean.  
 19 In this framework, tabular icebergs are represented by **non-levitating** Lagrangian elements  
 20 that **drift are submerged** in the ocean, and . The elements are held together and inter-  
 21 act with each other via bonds. A break of these bonds allows the model to emulate calv-  
 22 ing events (i.e. detachment of a tabular iceberg from an ice shelf) and tabular icebergs  
 23 breaking up into smaller pieces. Idealized simulations of a calving tabular iceberg, its  
 24 drift, and its breakup, demonstrate capabilities of the developed framework.

25 **1 Introduction**

26 Large tabular icebergs – pieces of floating ice with horizontal dimensions substan-  
 27 tially larger than the vertical dimension – calve infrequently ( $\sim$  every forty-fifty years)  
 28 from Antarctic or Greenlandic ice shelves [Jacobs et al, 1992]. Observational estimates  
 29 suggest that over the past 30 years approximately half of Antarctic ice-shelf decay is due  
 30 to iceberg calving, while the other half occurs through ice-shelf melting [Depoorter et  
 31 al, 2013; Rignot et al, 2013]. The infrequently-calved tabular icebergs (horizontal extent  
 32 larger than 5 km) account for more than 90% of the Southern Hemisphere iceberg mass  
 33 [Tournadre et al, 2016].

34 After calving, icebergs drift away from their origins, often becoming stuck in sea  
 35 ice, or grounding on bathymetric highs along the Antarctic coast [Lichy and Hellmer,  
 36 2001; Dowdeswell and Bamber, 2007]. Large tabular icebergs extend deep into the wa-  
 37 ter column, and have the potential to disrupt ocean circulation patterns for months or  
 38 even years after calving [Robinson et al, 2012; Stern et al, 2015]. The freshwater flux from  
 39 iceberg melt impacts ocean hydrography around the iceberg, influencing sea-ice produc-  
 40 tion and bottom-water formation [Arrigo et al, 2002; Robinson et al, 2012; Nicholls et  
 41 al, 2009; Fogwill et al, 2016]. Because of their large size, the tabular icebergs have long  
 42 lifetimes during which they drift over long distances injecting meltwater along the way  
 43 and impacting the Southern Ocean state (e.g. hydrography, sea-ice conditions, etc.) far  
 44 away from their calving origins [Stern et al, 2016; Rackow et al, 2017]. Meltwater injec-  
 45 tion (and the accompanying upwelling) from icebergs can also influence biological pro-  
 46 ductivity by bringing nutrients to the surface ocean or changing sea-ice conditions [Ar-  
 47 rigo et al, 2002; Vernet et al, 2012; Biddle et al, 2015]. The increased productivity as-  
 48 sociated with free-floating tabular icebergs has been linked with local increases in ocean  
 49 carbon uptake, potentially large enough to be a significant fraction of the Southern Ocean  
 50 carbon sequestration [Smith et al, 2007].

51 In recent years, there has been an increased interest in iceberg drift and decay. This  
 52 surge of interest has been driven by (i) the need to understand polar freshwater cycles  
 53 in order to create realistic climate change and sea level projections [Silva et al, 2006; Shep-  
 54 herd and Wingham, 2007; Rignot et al, 2013]; and (ii) the increased navigation and ex-  
 55 ploration activities in high-latitude iceberg-filled waters in the Arctic [Pizzolato et al,  
 56 2012; Unger, 2014; Henderson and Loe, 2016]. The increased interest in icebergs has led  
 57 to the development of numerical models of iceberg drift and decay [Mountain, 1980; Bigg  
 58 et al, 1997; Gladstone et al, 2001; Kubat et al, 2005], some of which have been included  
 59 in global General Circulation Models [Martin and Adcroft, 2010; Marsh et al, 2015]. These  
 60 iceberg drift models treat icebergs as **levitating** Lagrangian point particles, which are ad-  
 61 vected by the flow, and melt according to parameterizations for icebergs melt. Since ice-  
 62 bergs are treated as point particles, iceberg drift models are mostly suitable for mod-

eling icebergs smaller than an ocean grid cell. Consequently, these models have mostly been used to represent icebergs smaller than 3.5 km on a global scale [Jongma et al, 2009; Martin and Adcroft, 2010; Marsh et al, 2015].

Point-particle iceberg drift models are less suitable for modeling larger tabular icebergs, where the size and structure of the iceberg may be an important feature in determining their drift and decay [Stern et al, 2016]. They also are not suitable for studying the local effects that icebergs have on the surrounding ocean, or the small-scale processes that influence iceberg melt and decay [Wagner et al, 2014; Stern et al, 2015]. For these reasons, tabular icebergs are currently not represented in the iceberg drift models used as components of climate models, despite accounting for the vast majority of the total Southern Hemisphere iceberg mass [Tournadre et al, 2016]. Point-particle iceberg models also do not have any representation of iceberg breakup and calving, which is known to be an important iceberg decay mechanism that influences iceberg trajectories.

Some efforts have been made to modify levitating point-particle icebergs models so that they can be used to represent tabular icebergs [Lichy and Hellmer, 2001; Hunke, 2011; Rackow et al, 2017]. A promising approach involves integrating ocean properties over the implied iceberg surface area [Rackow et al, 2017] or implied iceberg depth [Hunke, 2011; Merino et al, 2016] when calculating the iceberg forcing (or applying iceberg melt fluxes), to account for the horizontal and vertical extent of the tabular iceberg. However, this approach does not account for influence that a submerged iceberg can have on the surrounding ocean due to its physical presence in the water column. Martin and Adcroft [2010] partially addressed this by allowing their icebergs to apply a pressure to top-most layer of their layered ocean model. This approach effectively allowed the icebergs to displace water, therefore making the point-particle icebergs non-levitating. A limitation of the Martin and Adcroft [2010] approach is that it the maximum iceberg size is constrained to be smaller than one ocean grid cell, which means that tabular icebergs can not be represented [Stern et al, 2016]. While it may be possible to combine these two approaches, at this stage more work is needed before point-particle icebergs can be used to represent tabular icebergs in climate models. Furthermore, at smaller scales and for regional modeling, it is clear that modeling tabular icebergs as point particle is not adequate to resolve the complex interactions between tabular icebergs and the surrounding ocean.

The goal of this study is to develop a new framework to model all kinds of icebergs, where tabular icebergs are explicitly resolved in the ocean. Our new representation of icebergs aims to include the following key properties: (i) icebergs should be able to travel large distances within the ocean, (ii) icebergs should melt and decay as they drift in the ocean, (iii) icebergs should behave as if they have finite extent **and have arbitrary shape and size** (in order to study local effects that icebergs have on the surrounding ocean), (iv) icebergs should be submerged in the ocean so they are not longer levitating, and (iv) tabular icebergs should be able to break away from ice shelves or break into smaller pieces. Properties (i) and (ii) are common to point-particle iceberg models, while properties (iii) **,(iv) and (v)** **and (iv)** are new to the framework developed in this study. A further requirement of the new framework is that the model should run sufficiently **quickly fast** to be used **included** in general circulation models used for climate.

In order to allow icebergs to travel large distances, we model the icebergs in a Lagrangian framework (as in the point particle iceberg drift models described above). However in our model icebergs are no longer treated as point particles that interact with the ocean at a single location. Instead icebergs are given physical structure, so that they interact with the ocean across multiple ocean grid cells, depress the ocean surface over a wide area, and can interact with other icebergs (Figure 1). This is done by assigning a finite surface area and shape to the Lagrangian elements, which allows the elements to behave as if they have a finite extent. The finite extent of an element is transmitted by the ocean by distributing the element's weight, surface area and melt fluxes over mul-

116 tiple ocean grid cells in a way which is consistent with the shape of the ice element. Finite-  
 117 extent elements interact with each other via repulsive forces which are applied when the  
 118 boundaries of the elements overlap. This prevents the icebergs from piling up on top of  
 119 one another, which has been an issue near coastlines in previous point-particle icebergs  
 120 models.

121 Large tabular icebergs can then be represented by ‘bonding’ together multiple ice  
 122 elements into larger structures using numerical bonds (Figure 1). The numerical bonds  
 123 hold the ice elements together and allow a collection of elements to move as a unit. This  
 124 allows tabular icebergs to drift in the ocean when forced by ocean currents and wind.  
 125 An advantage of representing tabular icebergs using numerical bonds is that by break-  
 126 ing the bonds, we can simulate iceberg calving (e.g.: Figure 2), or the response to an ice-  
 127 berg fracturing into multiple smaller pieces (see movies S1 and S2 in the Supporting In-  
 128 formation).

129 The manuscript is organized as follows. Section 2 gives a description of the key as-  
 130 pects of the model developed in this study. Since this model is a new approach to mod-  
 131 eling icebergs, we present technical aspects of the model. In Sections 3 and 4, we demon-  
 132 strate the capabilities of the model by simulating a tabular iceberg detaching from an  
 133 idealized ice shelf. In a further simulation we break some numerical bonds within the  
 134 tabular iceberg to demonstrate an iceberg splitting in two.

## 135 2 Model description

136 The Kinematic Iceberg Dynamics model (KID) is a Lagrangian particle-based model  
 137 in that the objects of the model are Lagrangian elements [Cundall and Strack, 1979; Lud-  
 138 ding, 2008; Radjai and Dubois, 2017]. Each element represents a column of ice that is float-  
 139 ing in the ocean, and has a position, velocity, mass, and a set of dimensions, which can  
 140 evolve in time. The motion of each element is determined by a momentum equation which  
 141 is solved in the (Lagrangian) reference frame of the element. The elements experience  
 142 oceanic and atmospheric forces, which are either prescribed, or computed by coupling  
 143 the iceberg model to an ocean/atmosphere model. The ice elements also interact with  
 144 one another via attractive and repulsive interactive forces, and can be bonded together  
 145 to form larger structures. The angular momentum of the elements is not modeled ex-  
 146 plicitly; instead rotational motion of larger structures emerge as a consequence of bond  
 147 orientation and collective motion.

148 In different contexts, the ice elements can be thought to represent individual ice-  
 149 bergs, sea-ice flows, or, when the elements are bonded together, they can represent larger  
 150 structures such as tabular icebergs or ice shelves.

151 The KID model is developed on the code base of an existing iceberg drift model  
 152 [Martin and Adcroft, 2010; Stern et al, 2016]. When run with the correct a different set  
 153 of runtime flags, the model runs as a traditional point-particle iceberg drift model.

### 154 2.1 Equations of motion

155 The elements drift in the ocean in response to atmosphere, ocean and sea-ice drag  
 156 forces, as well as the Coriolis force, a wave radiation force, a force due to the sea sur-  
 157 face slope and interactive forces with other elements. The momentum equation for each  
 158 element is given by

$$159 M \frac{D\vec{u}}{Dt} = \vec{F}_A + \vec{F}_W + \vec{F}_R + \vec{F}_C + \vec{F}_{SS} + \vec{F}_{SI} + \vec{F}_{IA}, \quad (1)$$

160 where  $\frac{D}{Dt}$  is the total (Lagrangian) derivative,  $M$  is the mass of the element,  $\vec{u}$  is the ve-  
 161 locity of the element, and the terms on the right hand side give the forces on the element

161 due to air drag ( $\vec{F}_A$ ), water drag ( $\vec{F}_W$ ), sea-ice drag ( $\vec{F}_{SI}$ ), Coriolis force ( $\vec{F}_C$ ), wave ra-  
162 diation force ( $\vec{F}_R$ ), sea surface slope ( $\vec{F}_{SS}$ ), and interactions with other elements ( $\vec{F}_{IA}$ ).

163 When ice elements move alone (without interactions with other elements), they can  
164 be thought of as representing individual (or clusters of) small icebergs, and follow the  
165 same equations described in the iceberg drift model of Martin and Adcroft [2010] (based  
166 on the equations outlined in Bigg et al [1997] and Gladstone et al [2001]). A description  
167 of these forces is provided for completeness in Appendix A.

168 In addition to the external forces, the ice elements experience interactive forces due  
169 to the presence of other elements. Two types of interactive forces are included between  
170 elements. The first force is a repulsive force which is applied to elements to prevent them  
171 from overlapping the boundaries of the neighboring elements. The second interactive force  
172 is a force due to numerical ‘bonds’, and is only applied if two elements are labelled as  
173 ‘bonded’. When two elements are bonded, each element feels an attractive force that pre-  
174 vents the elements from moving too far apart from one another. The details of the in-  
175 teractive forces are provided in below.

## 176 2.2 Interactive Forces

177 The interactive forces in the model are used to (i) prevent the ice elements from  
178 overlapping and (ii) to connect multiple ice elements together so that the collection of  
179 elements moves as a rigid body. Modeling the collisions and movements of rigid objects  
180 precisely, requires very small time steps and precise collision detection algorithms, which  
181 are very computationally expensive. Models using these methods are typically only run  
182 for a few days or even a few seconds, and are used to study rapid processes like crack  
183 formation or ridging [Hopkins, 2004; Bassis and Jacobs, 2013; Rabatel et al, 2015]. The  
184 tabular iceberg framework presented in this study is developed in order to be used in gen-  
185 eral circulation models used for multi-year simulations. In order to gain the required com-  
186 putational efficiency, we relax the requirement that icebergs must be perfectly rigid and  
187 that ice elements can not overlap. Instead, we model the interactive forces between ice  
188 elements using damped elastic forces, which can be calculated more efficiently.

189 The total interactive force on an element is calculated by adding together the in-  
190 teractions with all other elements, such that the interactive force on element  $i$ ,  $(\vec{F}_{IA})_i$   
191 is given by:

$$192 (\vec{F}_{IA})_i = \sum_{j \neq i} (\vec{F}_{IA})_{ij}, \quad (2)$$

193 where  $(\vec{F}_{IA})_{ij}$  is the force on element  $i$  by element  $j$ . Both bonded and repulsive inter-  
194 actions are modeled using elastic stresses with frictional damping. The elastic compo-  
195 nent of the force is a function of the distance between the two elements, while the fric-  
tional damping force depends on the relative velocity of the two elements.

196 To describe the forces between two elements, we begin by introducing some nota-  
197 tion. Let  $\vec{x}_i$ ,  $\vec{x}_j$  be the positions of elements  $i$  and  $j$ . The distance between elements  $i$   
198 and  $j$  is

$$199 d_{ij} = |\vec{x}_i - \vec{x}_j|. \quad (3)$$

200 In calculations of the interactive forces between elements, the elements are assumed to  
be circular. We define the interaction radius of an element by

$$201 R_i = \sqrt{\frac{A_i}{\pi}}, \quad (4)$$

202 where  $A_i$  is the planar surface area of element  $i$ . Using this, we define the critical-interactive-  
length scale,

$$203 L_{ij} = R_i + R_j, \quad (5)$$

204 which governs interactions between elements  $i$  and  $j$ . Repulsive forces are only applied  
when  $d_{ij} < L_{ij}$ , while for  $d_{ij} > L_{ij}$  attractive bonded forces are applied when a bond ex-

205   ists between element  $i$  and  $j$  (see diagram in Figure 3). The interactive forces are de-  
 206   signed such that (in the absence of other external forces) bonded particles will settle in  
 207   an equilibrium position where elements are separated by  $L_{ij}$ .

208   To aid in notation, we define a bond matrix  $B_{ij}$  such that  $B_{ij} = 1$  if elements  $i$   
 209   and  $j$  are bonded together and  $B_{ij} = 0$  otherwise. Using this notation, the interactive  
 210   force  $(\vec{F}_{IA})_{ij}$  on an element  $i$  by an element  $j$  is given by

$$(\vec{F}_{IA})_{ij} = \begin{cases} (\vec{F}_e)_{ij} + (\vec{F}_d)_{ij} & \text{if } (d_{ij} \leq L_{ij}) \text{ or } (d_{ij} > L_{ij} \text{ and } B_{ij} = 1) \\ 0 & \text{if } d_{ij} > L_{ij} \text{ and } B_{ij} = 0. \end{cases} \quad (6)$$

211    $(\vec{F}_e)_{ij}$  and  $(\vec{F}_d)_{ij}$  are the elastic and frictional damping components of the interactive  
 212   force between elements  $i$  and  $j$ . The elastic force  $(\vec{F}_e)_{ij}$  between elements is given by

$$(\vec{F}_e)_{ij} = -\kappa_e \left( d_{ij} - L_{ij} \right) M_{ij} \vec{r}_{ij}, \quad (7)$$

213   where  $\vec{r}_{ij} = \frac{(\vec{x}_i - \vec{x}_j)}{|\vec{x}_i - \vec{x}_j|}$  is the directional unit vector between the position of element  $i$  and  
 214    $j$ ,  $\kappa_e$  is the spring constant, and  $M_{ij}$  is the minimum of the masses of elements  $i$  and  $j$ .  
 215   The interactive forces obey Newton's 3rd Law (i.e.:  $(\vec{F}_{IA})_{ij} = -(\vec{F}_{IA})_{ji}$ ). The mini-  
 216   mum mass,  $M_{ij}$ , is preferred to the average mass, since this means that for two bonded  
 217   elements a fixed distance apart, the acceleration due to elastic forces is bounded, even  
 218   when the mass of one of the elements approaches zero.

219   The frictional damping force acts to dampen the relative motion of the two par-  
 220   ticles. If  $\vec{r}_{ij}^\perp$  is the direction vector perpendicular to  $\vec{r}_{ij}$ , and  $P_{\vec{r}_{ij}}$  and  $P_{\vec{r}_{ij}^\perp}$  are the pro-  
 221   jection matrixes that projects onto  $\vec{r}_{ij}$  and  $\vec{r}_{ij}^\perp$  respectively, then the frictional damp-  
 222   ing force is given by

$$(\vec{F}_d)_{ij} = -M_{ij} c_{r_{||}} P_{\vec{r}_{ij}} \cdot (\vec{u}_i - \vec{u}_j) \quad (8)$$

223   Here  $c_{r_{||}}$  and  $c_{r_\perp}$  are the drag coefficients for the damping motion parallel and perpendicular  
 224   to  $\vec{r}_{ij}$ , respectively. We set  $c_{r_{||}} = 2\sqrt{\kappa_e}$ , so that the elastic force parallel to  $\vec{r}_{ij}$  is crit-  
 225   ically damped. The perpendicular drag coefficient is set to  $c_{r_\perp} = \frac{1}{4} c_{r_{||}}$ . The perpendicular  
 226   damping force is used to reduce the relative motion of ice elements passing by one another  
 227   with overlapping boundaries. The damping forces are implemented using an implicit time  
 228   stepping scheme, to avoid stability issues for very small elements (details found in Ap-  
 229   pendix B).

230   Figure 4 illustrates the effectiveness of the repulsive forces in an uncoupled (ice-  
 231   only) simulation. In this simulation ice elements are forced westward into a bay, and even-  
 232   tually come to rest in the bay with a small amount of overlap between elements. The  
 233   amount of overlap between elements in the final state of the simulation depends on the  
 234   magnitude of the spring constant,  $\kappa_e$ , with larger spring constants reducing the amount  
 235   of overlap. Increasing the spring constant also makes the system numerically stiff so that  
 236   smaller time steps are required to prevent numerical instabilities (the system is stable  
 237   for time steps satisfying  $dt^2 < 4/\kappa_e$ ). A value of  $\kappa_e = 10^{-5}$  s<sup>-2</sup> is chosen that is large  
 238   enough to prevent too much overlap between elements for typical ocean forcings (e.g.: Fig-  
 239   ure 4), and small enough to allow for time steps up to 10 minutes (smaller time steps  
 240   are used when the model is coupled to an ocean model).

241   Figure 5 illustrates the effectiveness of the numerical bonds in simulations of small  
 242   icebergs (individual un-bonded elements) and large icebergs (constructed from many ice  
 243   elements bonded together) forced to drift towards a convex coast line. When the tab-  
 244   ular icebergs arrive at the coast, they bump into the coastline and begin to rotate, in-  
 245   fluencing the paths of the other icebergs. This example illustrates an advantage of us-  
 246   ing small elements bonded together to represent large-scale structure - i.e. rotational mo-  
 247   tion of large structures can be simulated without explicitly accounting for the angular  
 248   momentum of the elements (as discussed in Jakobsen [2001]). Movies of these uncoupled  
 249   simulations are found in S3 and S4 in the Supporting Information.

### 250      2.3 Initializing element geometry and packing

251      For purposes of initialization, we assume that elements have surface areas which  
 252      are shaped as equally-sized regular hexagons (note that the elements are assumed to be  
 253      circular for purposes of interactions). When packing elements together, the hexagonal  
 254      elements are initially arranged in a staggered lattice, with each element bonded to the  
 255      adjacent elements (Figures 1 and 6a). In this arrangement, each element (away from the  
 256      edges) is bonded to six other elements. The bonds between elements form a pattern of  
 257      equilateral triangles, which gives rigidity to the larger structure. The circular shape of  
 258      elements (used for interactions) is inscribed within the hexagonal shape used for pack-  
 259      ing (Figure 6a). The centers of adjacent elements are initially separated by a distance  
 260       $d_{ij} = L_{ij} = 2A_p$ , where  $A_p$  is the length of the apothems of the hexagons.

261      Some experiments were also performed using rectangular elements, arranged in a  
 262      regular (non-staggered) lattice. In this case, each element forms four bonds with adja-  
 263      cent elements. However, the resultant structures were found to be much less rigid and  
 264      tended to collapse when sufficient forces was **were** applied. For this reason, we only show  
 265      the results using hexagonal elements.

### 266      2.4 Ocean-ice and ice-ocean coupling

267      The KID model is coupled to the ocean model via a two-way synchronous coupling,  
 268      meaning that ocean-model fields are passed to the iceberg model, and iceberg model fields  
 269      are passed back to the ocean model at every time step. Passing fields between the two  
 270      models involves interpolating the fields from the ocean model's Eulerian grid onto the  
 271      iceberg model's 'Lagrangian grid' (i.e.: onto the ice elements), and aggregating fields from  
 272      the Lagrangian elements onto the ocean-model's Eulerian grid.

273      The coupling from the ocean model to the iceberg model is straight forward: at ev-  
 274      ery time step: the ocean mixed layer temperature, salinity, velocity and sea-ice concen-  
 275      tration are passed from the ocean model to the iceberg model, to be used in the momen-  
 276      tum and thermodynamic equations of the ice elements. Since tabular icebergs are ex-  
 277      plicitly resolved in the ocean, it is sufficient for each element to interact with ocean mixed  
 278      layer only (i.e.: there is no need to manually embed icebergs into the ocean by integrat-  
 279      ing ocean fields over the icebergs' thickness, as suggested in Merino et al [2016], or to  
 280      integrate ocean fields over an implied iceberg surface area, as suggested in Rackow et al  
 281      [2017]). Within the iceberg model, the ocean model fields are interpolated onto the La-  
 282      grangian grid using a bilinear interpolation scheme.

283      The iceberg model influences the ocean by: (i) applying a pressure to the ocean sur-  
 284      face, (ii) affecting the upper ocean by applying a no-slip boundary condition and fric-  
 285      tional velocity beneath the ice, and (iii) imposing heat, salt and mass fluxes on the ocean,  
 286      associated with ice melting. Six fields are passed from the iceberg model to the ocean  
 287      model: ice mass, ice area, frictional velocity, and heat, salt and mass fluxes. Fields in  
 288      the iceberg model are aggregated from the Lagrangian elements to the Eulerian ocean  
 289      grid before they are passed to the ocean model.

290      The aggregation of the iceberg-model fields onto the ocean grid is done in a way  
 291      that is consistent with the shape of the elements in the iceberg model (see Section 2.3).  
 292      Fields are 'spread' to the ocean model grid by exactly calculating what fraction of an  
 293      element's surface area lies in a particular grid box, and dividing the field in proportion  
 294      to this fraction. As an example, consider a hexagonal element in the iceberg model, which  
 295      is positioned such that it intersects four ocean grid cells (Figure 6b). In this situation,  
 296      the element's mass (for example) is divided between these four ocean cells in proportion  
 297      to the overlap area between the hexagonal element and the grid cell (this fraction is shown  
 298      by the colors in Figure 6b). An advantage of this approach is that there are no jumps

299 in pressure as an element moves from one grid cell to another, which could trigger ar-  
300 tificial tsunamis within the ocean model, making the ocean model unrealistic.

301 The numerical calculation of the intersection between hexagons and the ocean grid  
302 is simplified by dividing the hexagon into 6 equilateral triangles. This method allows for  
303 the intersection to be found even when the hexagon is not aligned with the grid.

304 The aggregation scheme is coded with the restriction that an element's area can  
305 only intersect a maximum of four ocean grid cells at a time. A consequence of this is that  
306 this sets a limit on the maximum size of elements that can be represented using this model,  
307 i.e., the longest horizontal dimension of an ice element must be smaller than the ocean  
308 grid spacing. Larger ice structures are constructed by bonding together smaller elements.

## 309 2.5 Melting parameterization

310 The ice elements change their mass and size due to melting, which also affects the  
311 surrounding ocean by changing its heat and salt content. In the model, these processes  
312 are parametrized in several ways. In this section we described the melt parametrization  
313 for bonded, unbonded and partially bonded elements.

314 As mentioned above, ice elements which do not interact with other elements are  
315 modeled identically to the point particle icebergs described in Martin and Adcroft [2010].  
316 These elements melt according to three semi-empirical parametrization for melt com-  
317 monly used in previous iceberg studies [Gladstone et al, 2001; Martin and Adcroft, 2010].  
318 Three types of iceberg melting are distinguished: basal melt,  $M_b$ , melt due to wave ero-  
319 sion,  $M_e$  and melt due to buoyant convection,  $M_v$ . The melt rates  $M_e$  and  $M_v$  are ap-  
320 plied to the sides of the ice element, while  $M_b$  is applied at the ice element base. The  
321 details of  $M_b$ .  $M_v$  and  $M_e$  are given in Appendix A.

322 When multiple elements are bonded together to form larger structures, it is no longer  
323 appropriate to use the melt parameterizations developed for individual point-particle ice-  
324 bergs. An element which is completely surrounded by other elements, is meant to rep-  
325 resent a column of ice in the middle of a large structure, and hence will not experience  
326 melt at its sides due to wave erosion or buoyant convection. Also, the iceberg basal melt  
327 rate,  $M_b$  described above is based on boundary layer theory of flow past a finite plate,  
328 and is only appropriate for basal surfaces where the distance from the leading edge is  
329 sufficiently small [Eckert, 1950; Weeks and Campbell, 1973]. For an element in the in-  
330 terior of a large structure, the distance from the edge of the structure is large, and so  
331 using  $M_b$  for the basal melt is not appropriate. Instead, the basal melt,  $M_s$  is determined  
332 using the three equation model for basal melt, which is a typical melting parametriza-  
333 tion used beneath ice shelves [Holland and Jenkins, 1999], and has been used to parametrize  
334 melt rates beneath large icebergs in previous studies [Silva et al, 2006; Rackow et al, 2017].

335 When using both individual elements and bonded elements in the same simulation,  
336 we determine which melt rate parameterizations to use based on the amount of bonds  
337 that each element has. An element in the center of a large structure has the maximum  
338 number of bonds, while an un-bonded element has no bonds. If an element can have max-  
339 imum number of bonds  $N_{\max}$ , and the number bonds that an element has is  $N_b$ , then  
340 the fraction of the element's perimeter surrounded by ocean (rather than by other ice  
341 elements) is estimated as  $\epsilon = 1 - \frac{N_b}{N_{\max}}$ . In this case, the element experi-  
342 ences side melt and bottom melt

343

$$M_{\text{side}} = \epsilon(M_v + M_e) \quad (9)$$

344 and

$$M_{\text{bottom}} = \epsilon M_b + (1 - \epsilon) M_s, \quad (10)$$

345 respectively. In this way, elements with no bonds (i.e.:  $\epsilon = 1$ ), melt like point-particle  
 346 icebergs; elements at the center of large structures (i.e.:  $\epsilon = 0$ ) melt like ice shelves; and  
 347 elements at the sides of large structures have a combination of iceberg side and basal melt,  
 348 and ice-shelf melt.

349 A similar procedure is used to allow elements at the edge of a large structures to  
 350 experience partial side drag and wave radiation forces, while for interior elements the side  
 351 drag force is zero. Details of are provided in Appendix A.

## 352 2.6 Algorithms and computational efficiency

353 Including interactions between elements leads to an increase in the computational  
 354 complexity of the model. In this subsection we comment on some of the algorithmic pro-  
 355 cedures that have been used to increase the computational efficiency.

### 356 2.6.1 Interactions and Bonds

357 At every time step, we calculate the force on each element due to interactions with  
 358 every other element. This involves order  $N^2$  operations (for N elements), which becomes  
 359 computational expensive as N grows large. We reduce the number of computations us-  
 360 ing a space-partitioning contact search where we leverage by leveraging the fact that each  
 361 element only has repulsive interactions with elements that are less than one ocean grid  
 362 cell away, and each element only has bonded interactions with a small number of other  
 363 elements.

364 The computation reduction is achieved by storing the element data in an efficient  
 365 way that eliminates a search through all element pairs to check if they are close to one  
 366 another or are bonded with one another. The data storage system is organized as fol-  
 367 lows: pointers to the memory structures containing each element are stored in linked list  
 368 data structures, which allow elements to be added and removed from the lists easily with-  
 369 out restructuring the entire list. Instead of using one list for all the elements on a pro-  
 370cessor (as was done in the original code [Martin and Adcroft, 2010]), we use a separate  
 371 linked list for each ocean grid cell. When an element moves between ocean grid cells, it  
 372 is removed from its original list and added to the list corresponding to its new ocean grid  
 373 cell. Since the area of elements has to be smaller than the area of an ocean grid cell, the  
 374 critical interaction length scale (equation 5) is less than the size of a grid cell. This means  
 375 that elements only experience repulsive forces with other elements in the same ocean grid  
 376 cell, or in one of the 8 adjacent cells. At each time step and for each element  $i$ , the code  
 377 traverses the linked lists of the 9 surrounding grid cells, and applies a repulsive force if  
 378  $d_{ij} < L_{ij}$  (whether the elements are bonded or not). Limiting the possible repulsive  
 379 interactions to elements in these 9 linked lists substantially reduces the computational  
 380 time needed to calculate the total interactive forces.

381 The attractive forces are computed in a the following way. Each bond is assigned  
 382 a piece of memory. Each bond is assigned two pieces of memory (one for each of the two  
 383 elements involved in the bond). Each ice element contains a linked list of each of its bonds  
 384 (typically up to six bonds per element). At every time step, the code traverses the lists  
 385 of bonded elements, and adds an attractive bonded force corresponding to these bonds  
 386 if  $d_{ij} > L_{ij}$  (the repulsive bonded force to be applied when  $d_{ij} < L_{ij}$  is already ac-  
 387 counted for by the procedure outlined in the previous paragraph). Having a list of bonds  
 388 stored with each element reduces the computations needed for bonded interactions from  
 389 order  $N^2$  to order N. Computing attractive forces separately from the repulsive forces  
 390 allows us to avoid checking whether two elements are bonded, which further increases  
 391 the computational efficiency.

392        **2.6.2 Parallelization and halos**

393        The iceberg model runs on multiple processors in parallel (using the same grid de-  
 394        composition as the ocean model). When elements move from an ocean cell on one pro-  
 395        processor to an ocean cell on a second processor, the memory has to be passed ~~from one processor~~  
 396        ~~the next, added and removed to the appropriate lists and the from one processor to the~~  
 397        ~~next, added to and removed from the appropriate lists, and the~~ memory has to be al-  
 398        located and deallocated correctly. Element interactions across the edge of processors are  
 399        handled using computational halos. A computational halo is a copy of the edge of a one  
 400        processor which is appended to the edge of a second processor, so that the first proces-  
 401        sor can interact with the second processor during a time step. Before each time step, el-  
 402        ements at the edges of each processor are copied onto the halos of adjacent processors  
 403        so that they can be used in calculating the interactive forces. After each time step, these  
 404        halos are emptied, and the process is repeated. These halo updates are one of the most  
 405        computationally expensive parts of the iceberg model. Details of how the bonds are bro-  
 406        ken and reconnected across processor boundaries are provided in Appendix C.

407        **2.6.3 Time stepping**

408        The elements in the iceberg model are advected using a semi-implicit velocity Ver-  
 409        let time-stepping scheme. The velocity Verlet time stepping scheme is commonly used  
 410        in discrete element models in video games because it is computational efficient and has  
 411        desirable stability properties [Jakobsen, 2001]. This time stepping scheme was preferred  
 412        to the Runge-Kutta 4, which was used in the iceberg model of Martin and Adcroft [2010]  
 413        since the Verlet time stepping only requires one calculation of the interactive forces once  
 414        per time step (while the Runge-Kutta scheme requires the interactive forces to be cal-  
 415        culated four times). Since the calculation of the interactive forces is one of the most com-  
 416        putationally expensive part of the algorithm, the Verlet scheme leads to a significant in-  
 417        crease in the computational efficiency of the model. The Verlet scheme used in the model  
 418        contains a modification of the original (fully explicit) velocity Verlet time stepping scheme  
 419        in that damping terms are treated implicitly (which increases the numerical stability).  
 420        The details of this adapted time stepping scheme are outlined in Appendix B.

421        **3 Experiment Setup**

422        The introduction of Lagrangian elements, numerical bonds and interpolation schemes  
 423        between the Eulerian and Lagrangian grids (discussed in Section 2) means that we now  
 424        have the tools to model large tabular icebergs submerged in the ocean. We demonstrate  
 425        this capability by simulating a tabular iceberg drifting away from an ice shelf in ~~an~~ ide-  
 426        alized setting.

427        **3.1 Model configuration**

428        We use the geometric setup of the Marine Ice Ocean Modeling Inter-comparison  
 429        Project (MISOMIP) [Asay-Davis et al, 2016]. The configuration consists of an idealized  
 430        ice shelf in a rectangular domain. The domain is  $L_x = 80$  km wide and  $L_y = 480$  km  
 431        long, and contains an ice shelf which is grounded on the south side of the domain and  
 432        has an ice front at  $y=650$  km. The ice thickness and bottom topography of this setup  
 433        are shown in Figure 7a and 7c respectively, with the grounding line position drawn in  
 434        for reference. The configuration is the same as that of the Ocean0 setup in the MISOMIP,  
 435        with a few minor changes to the ice-shelf geometry (see the Supporting Information for  
 436        details).

437      **3.2 Initializing Lagrangian elements:**

438      The idealized ice shelf is constructed out of Lagrangian ice elements. Ice elements  
 439      are hexagonal and are arranged in a regular staggered lattice (as discussed in Section  
 440      2.3). The sides of the hexagons are initialized with length  $S = 0.98$  km. Gaps along  
 441      the boundaries of the domain are filled in using smaller elements so that the total ice-  
 442      shelf area is preserved. These smaller elements are held stationary throughout the sim-  
 443      ulations, and are not bonded to other elements.

444      The initial mass of the ice elements is determined by a preprocessing inversion performed  
 445      before the model is run. The initial masses of the ice elements are calculated from the  
 446      gridded ice thickness field using bilinear interpolation, assuming a constant ice density  
 447       $\rho = 918$  kg/m<sup>3</sup>. When the model runs, the mass of elements is aggregated from the La-  
 448      grangian elements onto the Eulerian ocean grid (see Section 2.3), and is used to find the  
 449      surface pressure and ice draft (part of an ice column submerged into the ocean). The ice  
 450      draft calculated without the aggregation (treating elements as point masses) contains  
 451      large resolution-dependent grid artifacts (Figures 7b). These grid artifacts are much re-  
 452      duced after the mass-spreading aggregation is used (Figure 7c).

453      **3.3 Ocean model setup**

454      The KID model is coupled to the MOM6 ocean model [Hallberg et al, 2013]. The  
 455      ocean model configuration uses a vertical coordinate system which is a hybrid between  
 456      a sigma-level and a z-level coordinate. In particular, model layers deform underneath the  
 457      ice shelf as they would in a sigma-coordinate model, but collapse to zero thickness when  
 458      they intersect with bottom topography, as they would in a z-level model. The coordi-  
 459      nate system was achieved using the ALE regridding-remapping scheme [White et al, 2009].  
 460      The model uses a horizontal resolution of 2 km, and 72 vertical layers. All simulations  
 461      were repeated using the ocean model configured in isopycnal mode (results were simi-  
 462      lar and are not presented here).

463      Ocean parameters are as specified in the MISOMIP configuration [Asay-Davis et  
 464      al, 2016], and are shown in Table 1. The simulation is initially at rest, with horizontally  
 465      uniform initial ocean temperature and salinity profiles which vary linearly between spec-  
 466      ified surface and bottom values:  $T_{\text{top}} = -1.9^\circ$  C,  $T_{\text{bottom}} = 1.0^\circ$  C,  $S_{\text{top}} = 33.8$   
 467      psu,  $S_{\text{bottom}} = 34.7$  psu. The maximum ocean depth is  $H_{\text{ocean}} = 720$  m. A sponge  
 468      layer is used on the northern boundary of the domain, which relaxes the temperature  
 469      and salinity back to the initial temperature and salinity profile. The sponge layer has  
 470      length  $L_{\text{sponge}} = 10$  km, and has a relaxation time scale parameter  $T_{\text{sponge}} = 0.1$  days  
 471      at the northern boundary. The inverse of the relaxation time scale parameter drops lin-  
 472      early to zero over the length of the sponge layer. Melting is set to zero for ocean cells  
 473      where the ocean column thickness is less than 10m to avoid using more energy to melt  
 474      ice than is present in the water column.

475      **3.4 Spinup period:**

476      The model is spun up for 5 years with all ice elements being fixed. During spinup,  
 477      the injection of buoyant meltwater at the base of the ice shelf drives a clockwise circu-  
 478      lation within the domain (not shown). The circulation compares well with an identical  
 479      static ice-shelf experiment run using an Eulerian ice-shelf model [Goldberg et al, 2012].  
 480      A detailed comparison of the Lagrangian and Eulerian ice-shelf models is presented in  
 481      a separate study, and is not shown here.

482      **3.5 Iceberg calving:**

483      After spinup, a large tabular iceberg detaches from the ice shelf, and is allowed to  
 484      drift into the open ocean. Since the focus of this study is on developing a framework for  
 485      modeling tabular icebergs, we bypass the question of how to prescribe a physical calv-  
 486      ing law [Benn et all, 2007; Alley et al, 2008; Levermann et al, 2012; Bassis and Jacobs,  
 487      2013] by manually breaking off a semi-circular iceberg. This is achieved by allowing all  
 488      ice elements initially within a 14.4 km radius of the center of the ice front to move freely  
 489      while the other ice elements continue to be held stationary. Ice elements less than 12 km  
 490      from the center of the ice front, are bonded together to form a semi-circular tabular ice-  
 491      berg. A ring of elements whose distance,  $d$ , from the ice front center obeys  $12 \text{ km} \leq d \leq$   
 492      14.4 km, are allowed to move freely, but have all their bonds removed. Elements in this  
 493      half annulus represent fragments of the ice shelf which calve into small pieces during the  
 494      calving event.

495      After the spinup period, a wind stress  $\vec{\tau} = \langle \tau_x, \tau_y \rangle = \langle 0.05, 0.05 \rangle \frac{N}{m^2}$  is ap-  
 496      plied to drive the tabular iceberg away from the ice-shelf cavity. This is referred to as  
 497      the Control simulation. Perturbation experiments were also performed using other wind  
 498      stress values. Further perturbation experiments were performed by breaking some nu-  
 499      matical bonds in order to break the tabular iceberg into smaller pieces.

500      **4 Model Results**

501      After spinup of the Control simulation, the elements near the ice-shelf front are al-  
 502      lowed to move freely, and the icebergs begin to drift away from the ice shelf while fully  
 503      submerged in the ocean (see Figures 2 and 8, and the movie S1 in the Supporting In-  
 504      formation). At this point, the iceberg model and the ocean model are fully coupled: changes  
 505      to the iceberg position alter the top-of-ocean pressure and dynamical boundary condi-  
 506      tion; and changes to the iceberg melt rates alter the top-of-ocean temperature, salt and  
 507      mass fluxes. These changing ocean boundary conditions influence the ocean by trigger-  
 508      ing gravity waves, driving surface mixing, and affecting the ocean stratification. The evolv-  
 509      ing ocean velocities, temperatures and salinities feedback onto the ice elements by chang-  
 510      ing the force balance on the ice elements (leading to changes in the elements' position),  
 511      and altering the melt rates. The various feedbacks within this coupled system offer many  
 512      opportunities for the model to become unstable. The fact that the model is stable and  
 513      that we are able to simulate tabular icebergs moving in the ocean without the modeling  
 514      crashing and introducing artificial effects like tsunamis, is a non-trivial technical mile-  
 515      stone.

516      **4.1 Iceberg motion**

517      In the Control simulation, the semi-circular tabular iceberg moves as a cohesive unit  
 518      due to the presence of the numerical bonds, while the smaller ice fragments quickly dis-  
 519      perse (Figure 2). The tabular iceberg drifts towards the north east, driven by the wind  
 520      and steered by the Coriolis force. As the tabular iceberg drifts northwards, it rotates in  
 521      a counterclockwise direction (the direction of the Coriolis force in the Southern Hemis-  
 522      pHERE), and makes contact with the eastern boundary of the domain, before continu-  
 523      ing northward. Most of the smaller ice fragments also move to the northeast, but not  
 524      as a cohesive unit. Some of these element also move to other parts of the domain.

525      The direction (and speed) of the iceberg drift is largely determined by the wind speed  
 526      and direction. Perturbation experiments using different wind stresses show that for suf-  
 527      ficiently large winds, the tabular iceberg drifts to the north east when  $\tau_x > 0$ , and to  
 528      the north west when  $\tau_x < 0$  (not shown). For a purely zonal wind stress with  $|\tau_x| \leq$   
 529       $0.01 \frac{N}{m^2}$ , the iceberg does not move away from the ice shelf. When the wind is purely off-  
 530      shore ( $\tau_x = 0.0 \frac{N}{m^2}$ ), a meridional wind stress  $\tau_y \geq 0.05 \frac{N}{m^2}$  is needed to move the tab-

531       ular iceberg away from the ice shelf. While this result is partly an artifact of the cho-  
 532       sen shape of the calving iceberg, it is also consistent with Bassis and Jacobs [2013] who  
 533       noted that calving is a two step process consisting of (i) ice-shelf rifting that forms an  
 534       iceberg and (ii) iceberg detachment. The results here suggest that strong (cross-shore)  
 535       winds may be required to drive large tabular icebergs away from their source ice shelves.

## 536       **4.2 Breaking bonds**

537       The numerical bonds in the iceberg model enable the tabular iceberg to retain its  
 538       shape. This is demonstrated by comparing the Control simulation to an identical sim-  
 539       ulation where all numerical bonds have been removed (Figure 9, movie S5). In the bond-  
 540       free simulation, the ice elements disperse and the calved iceberg quickly loses its orig-  
 541       inal structure. This bond-free simulation does not adequately represent the tabular ice-  
 542       berg, since a tabular iceberg needs to be able to move long distances through the ocean  
 543       as a cohesive unit. This result motivates the inclusion of bonds in the iceberg model, even  
 544       though they are more computationally expensive than traditional point-iceberg models.

545       By breaking some (but not all) numerical bonds, we can simulate breaking of tab-  
 546       ular icebergs into smaller pieces. Figure 10 shows the results of an experiment which is  
 547       identical to the Control experiment, except that all numerical bonds that intersect the  
 548       line  $x = \frac{L_x}{2}$  have also been severed. This effectively cuts the large tabular iceberg into  
 549       two halves. As the icebergs drift northwards, the two halves of the tabular iceberg each  
 550       move as a cohesive unit, but they are able to move independently of one other (Figure  
 551       10, movie S2). The two large fragments initially move together, but begin to separate  
 552       after a few days. The breaking of a tabular iceberg has the additional effect of increas-  
 553       ing the total surface area of ice exposed to the ocean, thus increasing the total decay rate  
 554       of the icebergs.

## 555       **4.3 Ocean response**

556       Since the tabular iceberg is submerged in the ocean, the iceberg calving and drift  
 557       affects the surrounding ocean. In the Control simulation, as the tabular iceberg drifts  
 558       northward a warming of the surface waters is observed around the tabular iceberg, with  
 559       the largest warming occurring at the ice-shelf front and along the tabular iceberg's rounded  
 560       edge (Figure 2). This surface warming is caused by upwelling of the warmer waters from  
 561       beneath the ice shelf and iceberg. As the icebergs drifts away from the ice shelf, these  
 562       warmer waters remain at the surface, mapping out the iceberg wake (Figure 2). The mo-  
 563       tion of the tabular iceberg disturbs the ocean surface, which affects ocean velocities through  
 564       out the water column (Figure 11). The elevated shears around the tabular iceberg lead  
 565       to increased vertical mixing in the vicinity of the iceberg, which alters the stratification  
 566       of the water column (Figure 8), warming the upper ocean. The signature of upwelling  
 567       water in the wake of a drifting tabular iceberg bears some similarity to satellite obser-  
 568       vations of streaks of increased ocean color in the wake of tabular iceberg in the South-  
 569       ern Ocean [Duprat et al, 2016], suggesting that the increased productivity around ice-  
 570       bergs may be driven by upwelling water delivering nutrients to the surface.

571       The surface warming and increased ocean mixing observed around the iceberg are  
 572       in contrast to the cooling of the ocean surface and increased stratification reported around  
 573       melting icebergs in previous modeling studies using point-particle icebergs [Martin and  
 574       Adcroft, 2010; Stern et al, 2016; Marsh et al, 2015]. This difference results from the fact  
 575       that previous iceberg models used levitating icebergs with freshwater fluxes applied to  
 576       the ocean surface, while in our model the iceberg is fully submerged in the ocean. In gen-  
 577       eral the sea surface temperature response to the presence of an iceberg submerged in the  
 578       water column will likely depend on the ambient stratification around the iceberg and the  
 579       amount of entrainment into the iceberg meltwater plume. This result could have impor-  
 580       tant implications for the Southern Ocean, since the warming/cooling of surface waters

581 around icebergs can lead to large-scale changes to sea-ice concentrations and dense-water  
 582 production [Stern et al, 2016].

#### 583 4.4 Iceberg melt rates

584 The increased subsurface velocities and temperatures cause elevated melt rates at  
 585 the base of the ice shelf and iceberg (Figure 12). The largest melt rates are observed at  
 586 the newly calved ice-shelf front and on the rounded side of the tabular iceberg (Figure  
 587 12a), where the iceberg calving has created steep ice cliffs. These sharp ice fronts allow  
 588 for large ocean currents (Figure 12c), which drive the elevated melt rates. The elevated  
 589 melt rates act to smooth out the ice front over time, making the ice cliff less steep. While  
 590 this is likely a real **phenomenon** **phenomena** that could be observed in nature, we should  
 591 be wary of the modeled velocities at the ice cliffs, since large changes in ice thicknesses  
 592 are associated with numerical pressure gradient errors which can drive spurious motion.

593 The large melt rates along the ice edges are also partly driven by the fact that different  
 594 melt parametrization are used in the interior and edges of large ice structures (see  
 595 Section 2.5). Figure 13 shows the melt rates computed with (a) the 3-equation-model  
 596 parametrization [Holland and Jenkins, 1999], (b) point-particle-iceberg-melt parametriza-  
 597 tion [Gladstone et al, 2001], and (c) the mixed-melt-rate parametrization (introduced  
 598 in Section 2.5). The 3-equation-model melt rates (Figure 13a) are less than a third of  
 599 the size of those calculated using the point-particle-iceberg-melt parametrization (Fig-  
 600 ure 13b). **The point-particle-iceberg-melt is dominated by the wave erosion term, which**  
 601 **is an order of magnitude larger than the basal melt.** When the mixed-melt-rate parametriza-  
 602 tion is used (Figure 13c), the very high melt rates are only observed at the edges of ice  
 603 structures.

## 604 5 Summary

605 In this study we present a novel framework for simulating tabular icebergs in ocean  
 606 models, and representing icebergs with finite extent and structure **submerged in the ocean**.  
 607 In this framework, large tabular icebergs are represented by collections of Lagrangian  
 608 elements that are held together by numerical bonds. Each ice element is assigned a sur-  
 609 face area and shape, and can interact with the ocean and other elements in a way which  
 610 is consistent with the shape of the element. Such a representation allows tabular icebergs  
 611 to interact with the ocean across a wide area (larger than a grid cell), and individual ice  
 612 elements to behave as if they had a finite extent. This is in contrast to previous repre-  
 613 sentations of icebergs in numerical models [Jongma et al, 2009; Martin and Adcroft, 2010;  
 614 Marsh et al, 2015] that treat icebergs as point particles. Assigning a finite extent to el-  
 615 ements prevents icebergs from piling up on top of one another, which has been an issue  
 616 for previous point-particle iceberg models. Explicitly resolving tabular icebergs in the  
 617 ocean allows the icebergs **to be non-levitating and thus** to interact with the ocean in a  
 618 more realistic way, and allows us to study the effects that tabular icebergs have on ocean  
 619 circulation. Including numerical bonds between elements allows for simulations which  
 620 emulate iceberg calving and fracture by severing the bonds.

621 The capabilities of the tabular iceberg model are demonstrated by modeling a tab-  
 622 ular iceberg drifting away from an idealized ice shelf (also constructed using Lagrangian  
 623 elements). The results show that explicitly resolving tabular icebergs in the ocean al-  
 624 lows for a complex interaction between the iceberg and the surrounding ocean. In our  
 625 Control setup, a tabular iceberg is driven away from the ice shelf by ocean currents, wind  
 626 stress, and the Coriolis force. As the iceberg moves through the water, it disturbs the  
 627 ocean surface, driving ocean currents. The motion of the iceberg and melt beneath the  
 628 iceberg drive upwelling along the sides of the iceberg, which entrains ambient water and  
 629 causes a warming of the surface ocean in the wake of the iceberg. The changing ocean  
 630 conditions feed back onto the iceberg, affecting its motion and melt rates. The highest

631 melt rates are observed at the edge of the iceberg which has the steepest ice cliff. These  
 632 have the effect of smoothing out the ice edge over time. Simulations without using nu-  
 633 matical bonds showed that the bonds are essential for allowing the iceberg to move as  
 634 a unit. We also demonstrate that by breaking these numerical bonds we can simulate  
 635 iceberg fracture, which is an important process that increases the rate of iceberg decay.

636 To our knowledge, the model presented in this study is the first model to explic-  
 637 itly resolve drifting tabular icebergs in an ocean model that can be used for climate stud-  
 638 ies. A natural extension of this work is a representation of tabular icebergs in a general  
 639 circulation model (GCM). However, before this can be done, there are a number of is-  
 640 sues that need to be resolved: firstly, the question of how and when to introduce tab-  
 641 ular icebergs into the ocean needs to be addressed [Stern et al., 2016]. For GCM's with  
 642 active ice shelves, a calving law is needed to release the tabular iceberg into the ocean.  
 643 The question of what calving law to use is a topic of ongoing research [Benn et all, 2007;  
 644 Alley et al, 2008; Levermann et al, 2012; Bassis and Jacobs, 2013] and is still unresolved.  
 645 One potential way to temporarily bypass this problem would be to run hindcast simu-  
 646 lations using historically observed calving events. A related issue is the question of how  
 647 and when to break the bonds within the freely floating icebergs to simulate iceberg breakup.  
 648 Without a rule for iceberg breakup, the tabular icebergs would likely drift to unrealis-  
 649 tically low latitudes. Further work is also needed to understand (and model) the inter-  
 650 actions between tabular icebergs and sea ice, and to parametrize the effects of iceberg  
 651 grounding, as these interactions play a large role in dictating the trajectories of tabu-  
 652 lar icebergs. However, despite these remaining challenges, the technical framework de-  
 653 scribed in this article is potentially a useful step towards including tabular icebergs in  
 654 global GCM's.

## 655 6 Appendix A

### 656 6.1 Environmental forces on ice elements

657 The non-interactive forces on an ice element are as described in [Martin and Ad-  
 658 croft, 2010], with a small modification to drag forces and wave radiation force, included  
 659 to account for elements at the edge of large structures, which have a reduced surface area  
 660 exposed to the ocean. , and are repeated here for completeness. When modeling the mo-  
 661 mentum balance, the elements are assumed to be cuboids with time-evolving lengths,  
 662 widths and thicknesses. The length  $L$  and width  $W$  of an element are initially set as  $L = W = \sqrt{A_s}$ , and thereafter evolve dynamically.  $A_s$  is the planar surface area of the el-  
 663 ement. The cuboid shape is used so that the momentum balance of unbonded elements  
 664 is exactly as described in [Martin and Adcroft, 2010]. The mismatch between the cuboid  
 665 shape used in the momentum balance and the hexagonal shape used for spreading mass  
 666 onto the ocean grid introduces a small error. This error is likely to be small compared  
 667 to the uncertainty in the drag coefficients, melt parametrization and other uncertainties  
 668 built into a iceberg model.

670 The forces on an element due to air (a), ocean (o) and sea ice (si) drag are given  
 671 by

$$(672) \vec{F}_a = \rho_a (0.5 c_{a,v} W F + c_{a,h} L W) |\vec{u}_a - \vec{u}| (\vec{u}_a - \vec{u}), \quad (11)$$

$$(673) \vec{F}_o = \rho_o (0.5 c_{o,v} W (D - T_{si}) + c_{o,h} L W) |\vec{u}_o - \vec{u}| (\vec{u}_o - \vec{u}), \quad (12)$$

$$(674) \vec{F}_{si} = \rho_{si} (0.5 c_{si,v} W T_{si} F + c_{si,h} L W) |\vec{u}_{si} - \vec{u}| (\vec{u}_{si} - \vec{u}). \quad (13)$$

675 Here  $\rho_a$ ,  $\rho_o$ ,  $\rho_{si}$ , are the density of air, ocean and sea ice, respectively.  $c_{a,v}$ ,  $c_{o,v}$  and  $c_{si,v}$   
 676 are the vertical drag coefficients with air, ocean and sea ice, while  $c_{a,h}$ ,  $c_{o,h}$  and  $c_{si,h}$  are  
 677 the respective horizontal drag coefficients.  $\vec{u}_a$ ,  $\vec{u}_o$ ,  $\vec{u}_{si}$ , are the velocities of air, ocean and  
 678 sea ice, respectively.  $L$ ,  $W$ ,  $T$ ,  $F$  and  $D$  are the length, width, thickness, freeboard, and  
 679 draft of the ice element.  $L$  and  $W$  are defined such that  $L \geq W$ . The element thick-  
 ness is related to the draft and freeboard by  $T = F + D$  and  $D = \frac{\rho}{\rho_o} T$ , where  $\rho$  is the

ice element density.  $T_{si}$  is the sea-ice thickness. As discussed in Section 2.5,  $\epsilon$  is the fraction of element's perimeter surrounded by ocean, and is given by  $\epsilon = 1 - \frac{N_b}{N_{\max}}$ , where  $N_{\max}$  is the maximum number of bonds that an element form, and  $N_b$  is the number of bonds that the element forms.

The wave radiation force ( $\vec{F}_R$ ) is given by

$$\vec{F}_R = \epsilon \rho_o c_r g a \frac{WL}{W+L} \frac{\vec{u}_a}{|\vec{u}_a|} \min(a, F) \quad (14)$$

where  $g$  is the acceleration due to gravity,  $a$  is the wave amplitude empirically related to the wind speed by  $a = 0.010125|\vec{u}_a - \vec{u}_o|$ , and  $c_{wd}$  is the wave drag coefficient defined as

$$c_{wd} = 0.06 \min \left( \max \left[ 0, \frac{L - L_c}{L_t - L_c} \right], 1 \right), \quad (15)$$

where  $L_w = 0.32|\vec{u}_a - \vec{u}_o|^2$  is an empirical wave length,  $L_c = 0.125L_w$  is the cutoff length, and  $L_t = 0.25L_w$  is the upper limit.

The pressure gradient force is approximated as a force due to sea surface slope and given by

$$\vec{F}_{SS} = -Mg\vec{\nabla}\eta \quad (16)$$

where  $\eta$  is the sea surface height.

A parametrization for iceberg capsizing is applied for tall narrow ice elements. Elements are forced to capsize when the ratio  $\frac{W}{H} < \sqrt{6\alpha(1-\alpha)}$ , where  $\alpha = \frac{\rho}{\rho_o}$ . [Wagner et al, 2017]. When this occurs, W and H are instantaneously swapped. The iceberg capsizing parametrization used here is different from the one described in [Martin and Adcroft, 2010], which was found to be inappropriate for modeling icebergs with evolving dimensions [Wagner et al, 2017]. In our model capsizing is only permitted for unbonded elements.

## 6.2 Melt rate parametrization

As discussed in Section 2.5, unbounded ice elements in the iceberg model decay according to parameterizations for iceberg decay typically used in iceberg drift models [Martin and Adcroft, 2010], while ice elements within larger ice structures have only a basal melt given by the three equation model [Holland and Jenkins, 1999]. For the purposes of applying melt rates, we again assume that the elements are cuboids with time-evolving lengths, widths and thicknesses, as discussed in the previous subsection above.

For unbonded ice elements, the element thickness decays due to basal melt at a rate  $M_b$ , while the length and width of the elements decay as a result of melt due to wave erosion,  $M_e$ , and melt due to buoyant convection,  $M_v$ . Following Gladstone et al [2001] and Martin and Adcroft [2010], the basal melt rate, the 'melt' due to wave erosion wave erosion melt rate, and buoyant convection melt rate are parameterized by

$$M_b = 0.58|\vec{u} - \vec{u}_o|^{0.8} \frac{\tilde{T}_o - \tilde{T}}{L^{0.2}} \quad (17)$$

$$M_e = \frac{1}{12} S_s \left( 1 + \cos [\pi A_i^3] \right) \left( \tilde{T}_o + 2 \right), \quad (18)$$

$$M_v = \left( 7.62 \times 10^{-3} \right) \tilde{T}_o + \left( 1.29 \times 10^{-3} \right) \tilde{T}_o^2. \quad (19)$$

$\tilde{T}$  is the effective iceberg temperature and is set to  $\tilde{T} = -4^\circ\text{C}$ ,  $\tilde{T}_o$  is the temperature at the top of the ocean,  $A_i$  is the sea-ice area fraction, and  $S_s$  is the sea state, which is

716 given by the Beaufort scale

$$S_s = \frac{2}{3} |\vec{u}_a - \vec{u}_o|^{\frac{1}{2}} + \frac{1}{10} |\vec{u}_a - \vec{u}_o| \quad (20)$$

717 All three melt rates are in units of meters per day.

718 For elements inside larger structures, the melt due to wave erosion and melt due  
 719 to buoyant convection are set to zero, and the basal melt,  $M_s$ , is given by the standard  
 720 three equation model [Holland and Jenkins, 1999]: neglecting the heat flux in the ice,  
 721 the heat flux balance, salt flux balance and freezing point constraint at the ice-ocean in-  
 722 terface can be expressed as

$$LM_s = c_{po}\gamma_T |\vec{u}_o - \vec{u}| (T_o - T_b), \quad (21)$$

$$S_b M_s = \gamma_S |\vec{u}_o - \vec{u}| (S_o - S_b) \quad (22)$$

723 and

$$f(S_b, T_b, p_b) = 0. \quad (23)$$

724 Here  $T_o$  and  $S_o$  are the mixed layer temperature and salinity below the ice;  $T_b$ ,  $S_b$  and  
 725  $p_b$  are the temperature, salinity and pressure at the ice-ocean interface.  $c_{po} = 3974 \text{ J kg}^{-1} \text{ }^{\circ}\text{C}^{-1}$   
 726 is the specific heat of water, and  $L = 3.35 \times 10^5 \text{ J kg}^{-1}$  is the latent heat of ice fusion.  
 727  $\gamma_T$  and  $\gamma_S$  are the coefficients representing the transfer of heat and salt through the bound-  
 728 ary layer. The specific formulation of  $\gamma_T$  and  $\gamma_S$  can be found in [Holland and Jenkins,  
 729 1999]. The final equations is a constrain imposed by the equation of state, which relates  
 730 the pressure-dependent freezing temperature and salinity at the ice-ocean interface. The  
 731 basal melt rate  $M_s$  is found by solving this system of three equations numerically.  
 732

## 733 7 Appendix B

### 734 7.1 Modified Verlet Algorithm

735 The model uses a version velocity Verlet time-stepping algorithm, which has been  
 736 modified to allow part of the forcing to be calculated implicitly. The traditional veloc-  
 737 ity Verlet algorithm is commonly used in molecular dynamics, as it is simple to imple-  
 738 ment, second order accurate and computationally efficient [Swope et al, 1982; Omelyan  
 739 et al, 2002]. Here we modify the traditional scheme to allow for the drag forces to be mod-  
 740 eled implicitly, which prevents large accelerations for element's elements whose mass ap-  
 741 proaches zero. To do this, we include both an implicit and explicit acceleration,  $\vec{a} = \vec{a}^{\text{exp}} +$   
 742  $\vec{a}^{\text{imp}}$ . The explicit acceleration,  $\vec{a}^{\text{exp}}$ , includes all forcing terms which depend only on  
 743 the previous time step and the current position, while the implicit acceleration,  $\vec{a}^{\text{imp}}$ ,  
 744 includes forcing terms which depend on the velocity at the current time step (in partic-  
 745 ular the drag and Coriolis forces).

746 Using a time step of  $\Delta t$ , and subscripts to denote the time step (so that  $t_{n+1} =$   
 747  $t_n + \Delta t$ ), the modified velocity Verlet scheme can be written as:

- 748 1) Calculate updated position:  $\vec{x}_{n+1} = \vec{x}_n + \vec{u}_n \Delta t + \frac{\Delta t^2}{2} (\vec{a}_n^{\text{exp}} + \vec{a}_n^{\text{imp}}).$
- 749 2) Calculate  $\vec{a}_{n+1}^{\text{exp}}$
- 750 3) Calculate  $\vec{a}_{n+1}^{\text{imp}}$  and  $\vec{u}_{n+1} = \vec{u}_n + \frac{\Delta t}{2} (\vec{a}_n^{\text{exp}} + \vec{a}_{n+1}^{\text{exp}}) + (\Delta t) \vec{a}_{n+1}^{\text{imp}}$

751 This scheme reduces to the traditional velocity Verlet when  $\vec{a}^{\text{imp}}$  is set to zero. Note  
 752 that  $\vec{a}_{n+1}^{\text{exp}} = \vec{a}_{n+1}^{\text{exp}}(\vec{x}_{n+1}, t_n)$  is an explicit function of  $\vec{x}_{n+1}$  and other quantities eval-  
 753 uated at time  $t_n$ , while  $\vec{a}_{n+1}^{\text{imp}} = \vec{a}_{n+1}^{\text{imp}}(\vec{u}_{n+1}, \vec{x}_{n+1}, t_n)$  additionally depends on  $u_{n+1}$ , and

754 needs to be solved implicitly. For this reason in step three,  $\vec{a}_{n+1}^{\text{imp}}$  and  $\vec{u}_{n+1}$  need to be  
 755 solved simultaneously, as described in the next subsection.

756 In equation (1), the forces due to ocean drag, atmospheric drag and sea ice drag  
 757 are treated implicitly. The force due to sea surface slope and wave radiation are treated  
 758 explicitly. The Coriolis term is handled using the Crank-Nicolson scheme so that half  
 759 of the effect is implicit and half is explicit. The elastic part of the interactive forces is  
 760 treated explicitly, while the interactive damping is handled semi-implicitly in that the  
 761 drag force on element A by element B depends on the velocities of elements A and B eval-  
 762 uated at time  $t_{n+1}$  and  $t_n$ , respectively.

## 763 7.2 Solving for the velocity implicitly

764 Since this modified scheme contains some forcing terms which are handled implic-  
 765 itly,  $\vec{a}_{n+1}^{\text{imp}}$  and  $\vec{u}_{n+1}$  need to be calculated simultaneously. We demonstrate how this is  
 766 done, using a simplified one-dimensional version of equation (1), neglecting the atmo-  
 767 spheric drag, sea-ice drag and Coriolis force, so that the only implicitly treated term is  
 768 the ocean drag. In this demonstration, we use a superscript to denote the ocean drag  
 769 force,  $F^o$ , and ocean velocity,  $u^o$ , to avoid confusion with the subscripts indicating time  
 770 step. We also define an explicit force,  $F^{\text{exp}}$ , which accounts for all forces not proportional  
 771 to the element velocity. With these simplifications, the implicit and explicit accelerations  
 772 are

$$773 a^{\text{exp}} = \frac{1}{M}(F^{\text{exp}}) \quad (24)$$

$$774 a^{\text{imp}} = \frac{1}{M}(F^o) \quad (25)$$

775 The ocean drag force at time  $t_{n+1}$  is modeled (mostly) implicitly as

$$776 F_{n+1}^o = \tilde{c}^o |u_n^o - u_n| (u_n^o - u_{n+1}), \quad (26)$$

777 where  $\tilde{c}^o$  is the effective drag coefficient, accounting for the dimensions of the ice element  
 778 (see equation 12).

779 Step 3 of the modified velocity Verlet scheme can be rewritten by introducing an  
 780 intermediate velocity  $u^*$ , which only depends on the velocity and acceleration at time  
 781  $t_n$ ,

$$782 u_n^* = u_n + \frac{1}{2}(\Delta t)a_n^{\text{exp}}. \quad (27)$$

783 Using this, the updated velocity (Step 3) can be written

$$784 u_{n+1} = u_n^* + \frac{\Delta t}{2}a_{n+1}^{\text{exp}} + (\Delta t)a_{n+1}^{\text{imp}}. \quad (28)$$

785 Including the forcing terms into this equations gives

$$786 u_{n+1} = u_n^* + \frac{\Delta t}{2M}(F_{n+1}^{\text{exp}}) + \frac{\Delta t}{M} \left( c_w |u_n^o - u_n| (u_n^o - u_{n+1}) \right) \quad (29)$$

787 Solving for  $u(t_{n+1})$  in terms of quantities which only depend on the previous time step  
 788 gives

$$789 u_{n+1} = \frac{u_n^* + \frac{\Delta t}{2M}(F_{n+1}^{\text{exp}}) + \frac{\Delta t}{M} \left( c_w |u_n^o - u_n| (u_n^o) \right)}{\left( 1 + \frac{\Delta t}{M} c_w |u_n^o - u_n| \right)} \quad (30)$$

790 Recall that  $F_{n+1}^{\text{exp}}$  is an explicit function of  $x_{n+1}$  and other quantities evaluated at  $t_n$ , which  
 791 are already known at this point. Once the  $u_{n+1}$  has been found, it can be used to cal-  
 792 culate the explicit and implicit accelerations, which are required for the next time step.

Finally, we note that the the drag term (equation 26) is not entirely implicit, since the element velocity inside the absolute value is evaluated at time  $t_n$ , rather than at time  $t_{n+1}$ . This is done so that we can solve for the updated velocity analytically. One consequence of this is that it can give rise to a small oscillation in the element velocity. This oscillation is addressed by using a predictive corrective scheme: after solving for a first guess of the velocity at time  $t_{n+1}$ , this estimate of the velocity is used to update the estimate of the drag force (i.e.: inside the absolute value signs). This updated drag, can now be used to repeat the process described above to find an improved estimate of the velocity. We found that two iterations were sufficient to remove the unwanted oscillation.

The procedure described in this section is easily extended to include more forcing terms and two dimensions (where it involves inverting a  $2 \times 2$  matrix).

## 8 Appendix C

### Connecting bonds across processor boundaries

Since the model is parallelized across multiple **distributed-memory** processors, it often happens that two elements on different processes are bonded together. Keeping track of numerical bonds across processor boundaries requires a lot of book keeping. In this section we describe the how the model handles bonds across processor boundaries.

The basics of the bond bookkeeping work as follows: consider an element A and an element B that are bonded together. Each element has a copy of the bond (a piece of memory which describes the bond between the two elements), which is stored with the element. Let A-B be the bond stored by element A, and B-A be the bond stored by element B. Bond A-B contains a pointer which points to element B and bond B-A contains a pointer which points to element A.

Consider a situation where element A and B are originally on Processor 1, and then element B moves to Processor 2. When this occurs, the memory assigned to element B on processor 1 is removed, and is allocated on Processor 2. This means that the pointer to element B in bond A-B (stored in element A on Processor 1) is no longer assigned. Similarly, the pointer to element A in bond B-A (stored in element B on Processor 2) is no longer assigned. Before the next time step, a halo update occurs, so that there is a copy of element A in the halo of Processor 2 and a copy of element B in the halo of Processor 1. After the halo update, the bonds A-B and B-A have to be reconnected on both Processor 1 and 2. To aid in reconnecting the bonds, a copy of the grid cell number of element B is stored in the bond A-B and a copy of the grid cell number of element A is stored in the bond B-A. We refer to this as the ‘most recent address’. Before a bond is moved from one processor to another, the ‘most recent address’ is updated, so that the bond can be reconnected later. To reconnect bond A-B on Processor 1 (for example), we find the most recent address of element B, and search through the list of elements in the grid cell corresponding to the most recent address of element B until element B is found. The pointer to element B in bond A-B is reassigned, and the bond is said to be connected.

The reconnected bond A-B (stored in element A) is said to be working properly when the following four tests pass:

1. The pointer to element B is assigned on bond A-B.
2. The corresponding bond B-A exists on element B.
3. A pointer to element A exists in this bond B-A.
4. The element A which is being pointed to is the same element A where you started.

834 A useful tool for debugging the disconnecting and reconnecting bonds routines is that  
835 each element is assigned a unique number so that elements are easily identified.

836 **Acknowledgments**

837 This study is supported by awards NA08OAR4320752 and NA13OAR439 from the Na-  
838 tional Oceanic and Atmospheric Administration, U.S. Department of Commerce. Spe-  
839 cial thanks to Robert Hallberg who contributed to this study through many helpful con-  
840 versations. The statements, findings, conclusions, and recommendations are those of the  
841 authors and do not necessarily reflect the views of the National Oceanic and Atmospheric  
842 Administration, or the U.S. Department of Commerce. The simulations in this paper  
843 can be reproduced using the `model_code` and experimental setups found at [https://github.com/sternalon/Iceberg\\_repo](https://github.com/sternalon/Iceberg_repo).  
844 The iceberg model source code can be found at <https://github.com/NOAA-GFDL/icebergs>.  
845 The source code for the other model components can be found at <https://github.com/NOAA-GFDL>.

## 846 References

- 847 Asay-Davis, X. S., S. L. Cornford, B. K. Galton-Fenzi, R. M. Gladstone, G. H. Gud-  
 848 mundsson, D. M. Holland, P. R. Holland, and D. F. Martin (2016), Experimental  
 849 design for three interrelated marine ice sheet and ocean model intercomparison  
 850 projects: MISMIP v. 3 (MISMIP+), ISOMIP v. 2 (ISOMIP+) and MISOMIP v. 1  
 851 (MISOMIP1). *Geoscientific Model Development* 9, no. 7: 2471.
- 852 Arrigo, K. R., G. L. van Dijken, D. G. Ainley, M. A. Fahnestock, and T. Markus  
 853 (2002). Ecological impact of a large Antarctic iceberg. *Geophys. Res. Lett.*, 29(7).
- 854 Alley, R. B., H. J. Horgan, I. Joughin, K. M. Cuffey, T. K. Dupont, B. R. Parizek,  
 855 S. Anandakrishnan, and J. Bassis (2008), A simple law for ice-shelf calving. *Sci-  
 856 ence* 322, no. 5906, 1344-1344.
- 857 Bassis, J. N., and S. Jacobs (2013), Diverse calving patterns linked to glacier geom-  
 858 etry. *Nature Geoscience*, 6(10), 833-836.
- 859 Benn, D. I., C. R. Warren, and R. H. Mottram (2007). Calving processes and the  
 860 dynamics of calving glaciers. *Earth-Science Reviews*, 82(3), 143-179.
- 861 Bigg, G. R., Wadley, M. R., Stevens, D. P., and Johnson, J. A. (1997), Modeling the  
 862 dynamics and thermodynamics of icebergs. *Cold Regions Science and Technology*,  
 863 26(2), 113-135.
- 864 Borstad, C. P., A. Khazendar, E. Larour, M. Morlighem, E. Rignot, M. P. Schodlok,  
 865 and H. Seroussi (2012), A damage mechanics assessment of the Larsen B ice shelf  
 866 prior to collapse: Toward a physically-based calving law, *Geophys. Res. Lett.*, 39,  
 867 L18502
- 868 Biddle, L. C., J. Kaiser, K. J. Heywood, A. F. Thompson and A. Jenkins (2015),  
 869 Ocean glider observations of iceberg-enhanced biological productivity in the north-  
 870 western Weddell Sea, *Geophys. Res. Lett.*, 42, 459465.
- 871 Cundall, P. A and O. D. L. Strack (1979), A discrete numerical model for granular  
 872 assemblies. *Geotechnique* 29, pp. 4765
- 873 De Rydt, J., and G. H. Gudmundsson (2016), Coupled ice shelf ocean modeling and  
 874 complex grounding line retreat from a seabed ridge. *J. of Geophys. Res.: Earth  
 875 Surface*, 121(5), 865-880.
- 876 Dunne, J.P., J.G. John,, A.J. Adcroft, S.M. Griffies, R.W. Hallberg, E. Shevliakova,  
 877 R.J. Stouffer, W. Cooke, K.A. Dunne, M.J Harrison, and J.P. Krasting (2012),  
 878 GFDL's ESM2 global coupled climate-carbon Earth System Models. Part I: Phys-  
 879 ical formulation and baseline simulation characteristics. *J. of Climate*, 25(19),  
 880 6646-6665.
- 881 Depoorter, M. A., J. L. Bamber, J. A. Griggs, J. T. M. Lenaerts, Stefan RM Ligten-  
 882 berg, M. R. van den Broek, and G. Moholdt (2013), Calving fluxes and basal melt  
 883 rates of Antarctic ice shelves. *Nature*, 502(7469), 89-92.
- 884 Determan J., Gerdes R. (1994), Melting and freezing beneath ice shelves: impli-  
 885 cations from a three-dimensional ocean-circulation model. *Ann. Glaciol.*, 20,  
 886 413-419.
- 887 Dowdeswell, J. A., and J. L. Bamber (2007), Keel depths of modern Antarctic ice-  
 888 bergs and implications for sea-floor scouring in the geological record. *Marine  
 889 Geology*, 243(1), 120-131.
- 890 Duprat, L. P., G. R. Bigg, and D. J. Wilton (2016), Enhanced Southern Ocean  
 891 marine productivity due to fertilization by giant icebergs. *Nature Geoscience*.
- 892 Eckert, E. R. G. (1950). Introduction to the Transfer of Heat and Mass. McGraw-  
 893 Hill.
- 894 Fogwill, C.J., E. van Sebille, E.A. Cougnon, C.S. Turney, S.R. Rintoul, B.K. Galton-  
 895 Fenzi, G.F. Clark, E.M. Marzinelli, E.B. Rainsley, and L. Carter (2016), Brief  
 896 communication: Impacts of a developing polynya off Commonwealth Bay, East  
 897 Antarctica, triggered by grounding of iceberg B09B. *The Cryosphere*, 10(6),  
 898 p.2603.

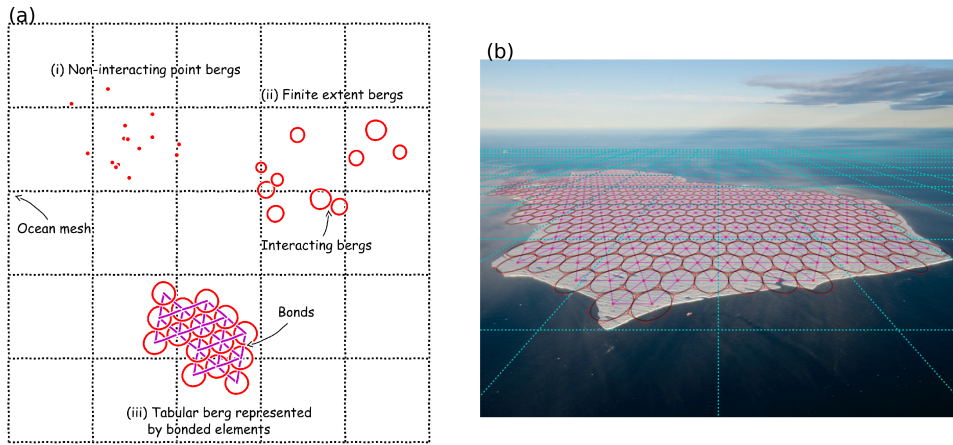
- 899 Gladstone, R. M., G. R. Bigg, and K. W. Nicholls. (2001), Iceberg trajectory mod-  
 900 eling and meltwater injection in the Southern Ocean (19782012). *J. of Geophys.*  
 901 *Res.: Oceans*, 106(C9), 19903-19915.
- 902 Goldberg, D. N., C. M. Little, O. V. Sergienko, A. Gnanadesikan, R. Hallberg, and  
 903 M. Oppenheimer (2012), Investigation of land ice?ocean interaction with a fully  
 904 coupled ice-ocean model: 1. Model description and behavior. *J. of Geophys. Res.:*  
 905 *Earth Surface*, 117(F2).
- 906 Gladish, C. V., D. M. Holland, P. R. Holland, and S. F. Price (2012), Ice-shelf basal  
 907 channels in a coupled ice/ocean model. *J. of Glaciol.*, 58(212), 1227-1244.
- 908 Grosfeld K., R. Gerdes, J. Determan (1997), Thermohaline circulation and interac-  
 909 tion between ice shelf cavities and the adjacent open ocean. *J. Phys. Oceanogr.*,  
 910 **102**, C7, 15959-15610.
- 911 Grosfeld, K., and H. Sandhger, (2004). The evolution of a coupled ice shelfocean sys-  
 912 tem under different climate states. *Global and Planetary Change*, 42(1), 107-132.
- 913 Hallberg, R., A. Adcroft, J. P. Dunne, J. P., Krasting, R. J., and Stouffer (2013),  
 914 Sensitivity of twenty-first-century global-mean steric sea level rise to ocean model  
 915 formulation. *J. of Climate*, 26(9), 2947-2956.
- 916 Holland D. M., Jenkins A. (2001), Adaptation of an isopycnic coordinate ocean  
 917 model for the study of circulation beneath ice shelves. *Mon. Wea. Rev.*, 129, 1905-  
 918 1927.
- 919 Holland P. R. and D. L. Feltham (2006), The effects of rotation and ice shelf topog-  
 920 raphy on frazil-laden Ice Shelf Water plumes. *J. Phys. Oceanogr.*, 36, 2312-2327.
- 921 Holland, D. M., and A. Jenkins (1999), Modeling thermodynamic ice-ocean interac-  
 922 tions at the base of an ice shelf. *J. of Phys. Oceanogr.* 29.8, 1787-1800.
- 923 Hellmer H.H., Olbers D. J. (1989), A two-dimensional model for the thermohaline  
 924 circulation under an ice shelf. *Antarctic Science*, 1, 325- 336.
- 925 Henderson J., J. S. P. Loe (2016), The Prospects andChallenges for Arctic Oil De-  
 926 velopment. *Oil, Gas and Energy Law Journal (OGEL)*, 14 (2)
- 927 Hopkins, M. A. (1996). On the mesoscale interaction of lead ice and floes. *J. of*  
 928 *Geophys. Res.: Oceans*, 101(C8), 18315-18326.
- 929 Hopkins, M. A. (2004). A discrete element Lagrangian sea ice model. *Engineering*  
 930 *Computations*, 21(2/3/4), 409-421.
- 931 Hunke, Elizabeth C., and Darin Comeau (2011), Sea ice and iceberg dynamic inter-  
 932 action. *J. of Geophys. Res.: Oceans* 116, C5.
- 933 Gaskill, H. S., and J. Rochester (1984). A new technique for iceberg drift prediction.  
 934 *Cold Reg. Sci. Technol.*, 8(3), 223-234.
- 935 Jacobs, S. S., H. H. Helmer, C. S. M. Doake, A. Jenkins, R. M. Frolich (1992), Melting  
 936 of ice shelves and the mass balance of Antarctica. *J. of Glaciol.*, 38(130),  
 937 375-387.
- 938 Jakobsen, T. (2001). Advanced character physics. In *Game Developers Conference*,  
 939 Vol. 3.
- 940 Jenkins, A., P. Dutrieux, S. S. Jacobs, S. D. McPhail, J. R. Perrett, A. T. Webb,  
 941 and D. White (2010), Observations beneath Pine Island Glacier in West Antarc-  
 942 tica and implications for its retreat. it *Nature Geo.*, 3(7), 468-472.
- 943 Jacobs, S. S., A. Jenkins, C. F. Giulivi, and P. Dutrieux (2011). Stronger ocean cir-  
 944 culation and increased melting under Pine Island Glacier ice shelf. *Nature Geo.*,  
 945 4(8), 519-523.
- 946 Jongma, J. I., E. Driesschaert, T. Fichefet, H. Goosse, and H. Renssen (2009), The  
 947 effect of dynamic-thermodynamic icebergs on the Southern Ocean climate in a  
 948 three-dimensional model, *Ocean Modell.*, 26, 104113.
- 949 Kubat I., M. Sayed, S. Savage, T. Carrieres (2005), An operational model of iceberg  
 950 drift *Int. J. Off. Polar Eng.*, 15 (2), 125131
- 951 Lewis E.L. and R.G. Perkin (1986), Ice pumps and their rates. *J. of Geophys. Res.*,  
 952 91, 11756-11762.

- 953 Losch, M. (2008). Modeling ice shelf cavities in a z coordinate ocean general circulation model. *J. of Geophys. Res.: Oceans*, 113(C8).
- 954
- 955 Li, B., H. Li, Y. Liu, A. Wang and S. Ji (2014), A modified discrete element model  
956 for sea ice dynamics. *Acta Oceanologica Sinica*, 33(1), 56-63.
- 957 Liu, M. B. and G. R. Liu (2010), Smoothed particle hydrodynamics (SPH): an  
958 overview and recent developments. *Archives of computational methods in engineering*,  
959 17(1), 25-76.
- 960 Lichéy, C., and H. H. Hellmer (2001). Modeling giant-iceberg drift under the influence  
961 of sea ice in the Weddell Sea, Antarctica. *J. of Glaciol.*, 47(158), 452-460.
- 962 Levermann, A., T. Albrecht, R. Winkelmann, M. A. Martin, M. Haseloff, and I.  
963 Joughin. (2012), Kinematic first-order calving law implies potential for abrupt  
964 ice-shelf retreat. *The Cryosphere*, 6(2), 273-286.
- 965 Luding, S. (2008), Introduction to discrete element methods: basic of contact force  
966 models and how to perform the micro-macro transition to continuum theory.  
967 *European Journal of Environmental and Civil Engineering* 12.7-8, pp. 785826
- 968 Mountain, D. G. (1980). On predicting iceberg drift. *Cold Reg. Sci. Technol.*, 1(3-4),  
969 273-282.
- 970 Martin, T., and Adcroft, A. (2010), Parameterizing the fresh-water flux from land  
971 ice to ocean with interactive icebergs in a coupled climate model. *Ocean Modelling*,  
972 34(3), 111-124.
- 973 Marsh, R., V. O. Ivchenko, N. Skliris, S. Alderson, G. R. Bigg, G. Madec, A. T.  
974 Blaker Y. Aksenov, B. Sinha, A.C. Coward, and J.L. Sommer (2015), NEMOICB  
975 (v1. 0): interactive icebergs in the NEMO ocean model globally configured at  
976 eddy-permitting resolution. *Geoscientific Model Development* 8, no. 5 (2015):  
977 1547-1562.
- 978 MacAyeal D.R. (1984), Thermohaline Circulation Below the Ross Ice Shelf: A Con-  
979 sequence of Tidally Induced Vertical Mixing and Basal Melting. *J. Geophys. Res.*,  
980 89, 597-606
- 981 Merino, N., Le Sommer, J., Durand, G., Jourdain, N. C., Madec, G., Mathiot, P.,  
982 and Tournadre, J. (2016), Antarctic icebergs melt over the Southern Ocean: cli-  
983 matology and impact on sea ice. *Ocean Modelling*, 104, 99-110.
- 984 Nicholls K.W. (1996), Temperature variability beneath Ronne Ice Shelf, Antarctica,  
985 from thermistor cables. *J. Phys. Oceanogr.*, 11, 1199-1210.
- 986 Nicholls KW, Østerhus S, Makinson K (2009), Ice-Ocean processes over the con-  
987 tinental shelf of the southern Weddell Sea, Antarctica: a review. *Rev. Geophys.*  
988 47(3).
- 989 Omelyan, I. P., M. I. Mryglod, and R. Folk (2002), Optimized Verlet-like algorithms  
990 for molecular dynamics simulations. *Physical Review E*, 65(5), 056706.
- 991 Pizzolato, L., S. E. Howell, C. Derksen, J. Dawson, L. Copland (2014), Changing  
992 sea ice conditions and marine transportation activity in Canadian Arctic waters  
993 between 1990 and 2012, *Climatic Change* 123 (2), 161173.
- 994 Pan, W., A. M. Tartakovsky, and J. J. Monaghan (2013). Smoothed particle hydro-  
995 dynamics non-Newtonian model for ice-sheet and ice-shelf dynamics. *J. of Comp.*  
996 *Phys.*, 242, 828-842.
- 997 Pralong, A., and M. Funk (2005), Dynamic damage model of crevasse opening and  
998 application to glacier calving, *J. Geophys. Res.*, 110, B01309.
- 999 Rabatel, M., S. Labb and J. Weiss (2015), Dynamics of an assembly of rigid ice  
1000 floes. *J. of Geophys. Res.: Oceans*, 120(9), 5887-5909.
- 1001 Rackow, T., C. Wesche, R. Timmermann, H. H. Hellmer, S. Juricke and T.  
1002 Jung (2017), A simulation of small to giant Antarctic iceberg evolution: dif-  
1003 ferential impact on climatology estimates. *J. of Geophys. Res.: Oceans*, doi:  
1004 10.1002/2016JC012513
- 1005 Radjai, F. and F. Dubois (2011), Discrete-Element Modeling of Granular Materials.  
1006 Wiley-Iste, p. 425

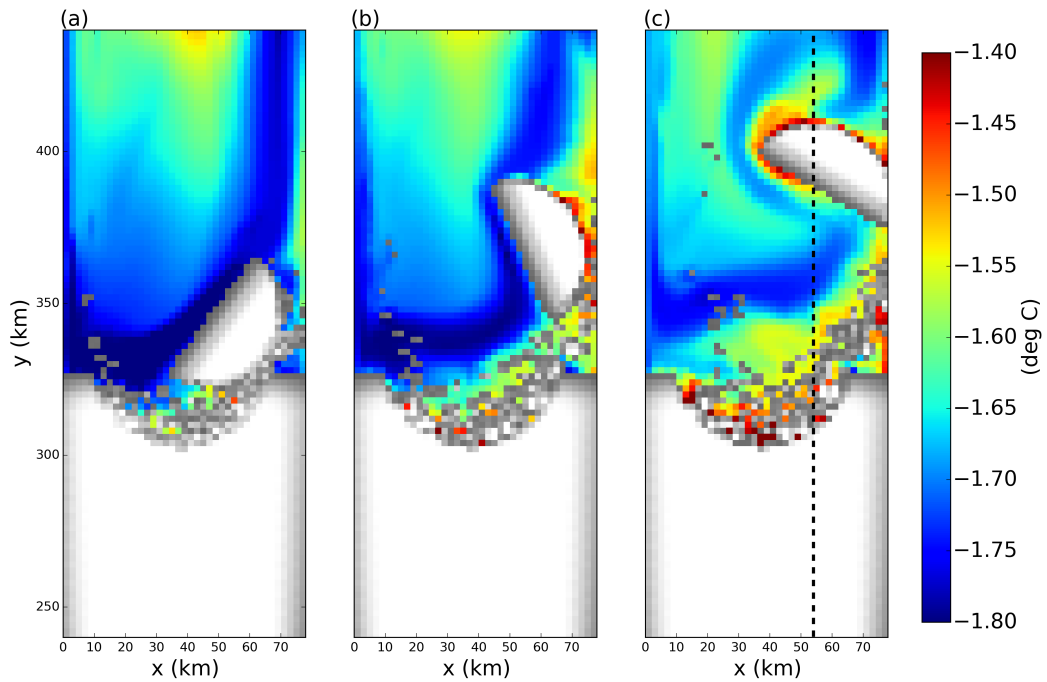
- 1007 Rignot, E., S. Jacobs, J. Mouginot, and B. Scheuchl (2013), Ice-shelf melting around  
 1008 Antarctica. *Science*, 341, no. 6143 (2013): 266-270.
- 1009 Robinson, N. J., M. J. M. Williams, P. J. Barrett, and A. R. Pyne (2010), Observa-  
 1010 tions of flow and ice-ocean interaction beneath the McMurdo Ice Shelf, Antarctica,  
 1011 *J. Geophys. Res.*, 115, C03025
- 1012 Sergienko, O. V. (2013). Basal channels on ice shelves. *J. of Geophys. Res.: Earth*  
 1013 *Surface*, 118(3), 1342-1355.
- 1014 Silva, T. A. M., Bigg, G. R., and Nicholls, K. W. (2006), Contribution of giant  
 1015 icebergs to the Southern Ocean freshwater flux. *J. of Geophys. Res.: Oceans*,  
 1016 111(C3).
- 1017 Smith, K., B. Robison, J. Helly, R. Kaufmann, H. Ruhl, H., T. Shaw, and M. Vernet  
 1018 (2007), Free-drifting icebergs: Hotspots of chemical and biological enrichment in  
 1019 the Weddell Sea, *Science*, 317, 478482.
- 1020 Shepherd, A., and D. Wingham (2007). Recent sea-level contributions of the Antarc-  
 1021 tic and Greenland ice sheets. *Science*, 315(5818), 1529-1532.
- 1022 Stern, A., D. M. Holland, P. R. Holland, A. Jenkins and J. Sommeria (2014), The  
 1023 effect of geometry on ice shelf ocean cavity ventilation: a laboratory experiment.  
 1024 *Experiments in Fluids*, 55(5), 1-19.
- 1025 Stern, A., Johnson, E., Holland, D.M., Wagner, T.J., Wadhams, P., Bates, R.,  
 1026 Abrahamsen, E.P., Nicholls, K.W., Crawford, A., Gagnon, J. and Tremblay, J.E.  
 1027 (2015), Wind-driven upwelling around grounded tabular icebergs. *J. of Geophys.*  
 1028 *Res.: Oceans*, 120(8), 5820-5835.
- 1029 Stern, A., A. Adcroft, and O. Sergienko (2016), The effects of Antarctic iceberg  
 1030 calving size distribution in a global climate model. *J. of Geophys. Res.: Oceans*,  
 1031 121(8), 5773-5788.
- 1032 Swope, W. C., H. C. Andersen, P. H. Berens, and K. R. Wilson (1982), A computer  
 1033 simulation method for the calculation of equilibrium constants for the formation of  
 1034 physical clusters of molecules: Application to small water clusters. *The Journal of*  
 1035 *Chemical Physics* 76, no. 1, 637-649.
- 1036 Tournadre, J., N. Bouhier, F. Girard-Ardhuin, and F. Rmy (2016), Antarctic ice-  
 1037 bergs distributions 1992-2014. *J. Geophys Res: Oceans*.
- 1038 Turnbull I.D., N. Fournier, M. Stolwijk, T. Fosnaes, D. McGonigal (2015), Opera-  
 1039 tional iceberg drift forecasting in Northwest Greenland, *Cold Reg. Sci. Technol.*  
 1040 110, 1-18
- 1041 Unger, J. D., 2014. Regulating the Arctic Gold Rush: Recommended Regulatory Re-  
 1042 forms to Protect Alaska's Arctic Environment from Offshore Oil Drilling Pollution  
 1043 . *Alaska L. Rev*, 31
- 1044 Vernet, M., et al. (2012), Islands of ice: Influence of free-drifting Antarctic icebergs  
 1045 on pelagic marine ecosystems, *Oceanography*, 25(3), 3839
- 1046 Wagner, T. J. W., P. Wadhams, R. Bates, P. Elosegui, A. Stern, D. Vella, E. P.  
 1047 Abrahamsen, A. Crawford, and K. W. Nicholls (2014), The footloose mechanism:  
 1048 Iceberg decay from hydrostatic stresses. *Geophys. Res. Lett.*, 41(15), 5522-5529.
- 1049 Wagner, T. J., A. A. Stern, R. W. Dell, and I. Eisenman (2017), On the representa-  
 1050 tion of capsizing in iceberg models. arXiv preprint arXiv:1702.06870.
- 1051 Weeks, W. F., and W. J. Campbell (1973). Icebergs as a fresh-water source: an  
 1052 appraisal. *J. of Glaciol.*, 12(65), 207-233.
- 1053 White, L., A. Adcroft, and R. Hallberg (2009), High-order regridding-remapping  
 1054 schemes for continuous isopycnal and generalized coordinates in ocean models. *J.*  
 1055 *of Comp. Phys.*, 228(23), 8665-8692.

Parameter	Symbol	Value	Unit
Domain Length	$L_x$	80	km
Domain Width	$L_y$	480	km
Horizontal Resolution	$\Delta x$	2	km
Number of vertical layers	$N_l$	72	non-dim
Horizontal Viscosity	$\nu_H$	6.0	$m^2 s^{-1}$
Diapycnal Viscosity	$\nu_V$	$10^{-3}$	$m^2 s^{-1}$
Horizontal Diffusivity	$\epsilon_H$	1.0	$m^2 s^{-1}$
Diapycnal Diffusivity	$\epsilon_V$	$5 \times 10^{-5}$	$m^2 s^{-1}$
Initial Surface Temperature	$T_t$	-1.9	$^{\circ}C$
Initial Bottom Temperature	$T_b$	1.0	$^{\circ}C$
Initial Surface Salinity	$S_t$	33.8	psu
Initial Bottom Salinity	$S_b$	34.7	psu
Maximum Ocean depth	$H_{ocean}$	720	m
Relaxation Time of Sponge Layer	$T_{sponge}$	0.1	days
Length of Sponge Layer	$L_{sponge}$	10	km
Ocean and iceberg model time step	$dt$	10	s
Elastic interactive force spring constant	$\kappa_e$	$10^{-5}$	$kg s^{-2}$

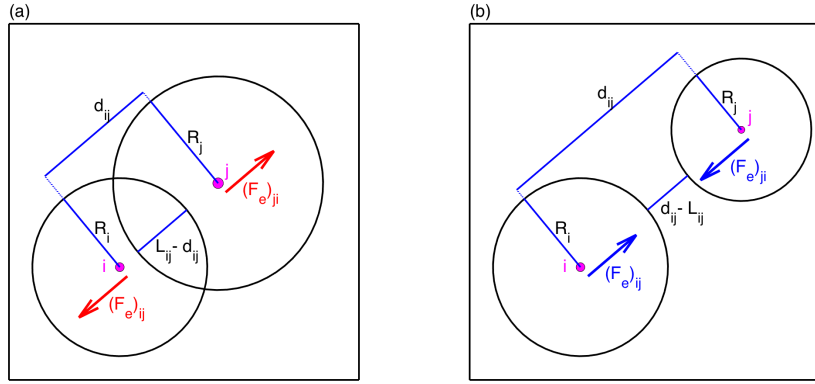
1056    **Table 1.** Parameters used in the model. The ocean model parameters are as described in  
 1057    Asay-Davis et al [2016]



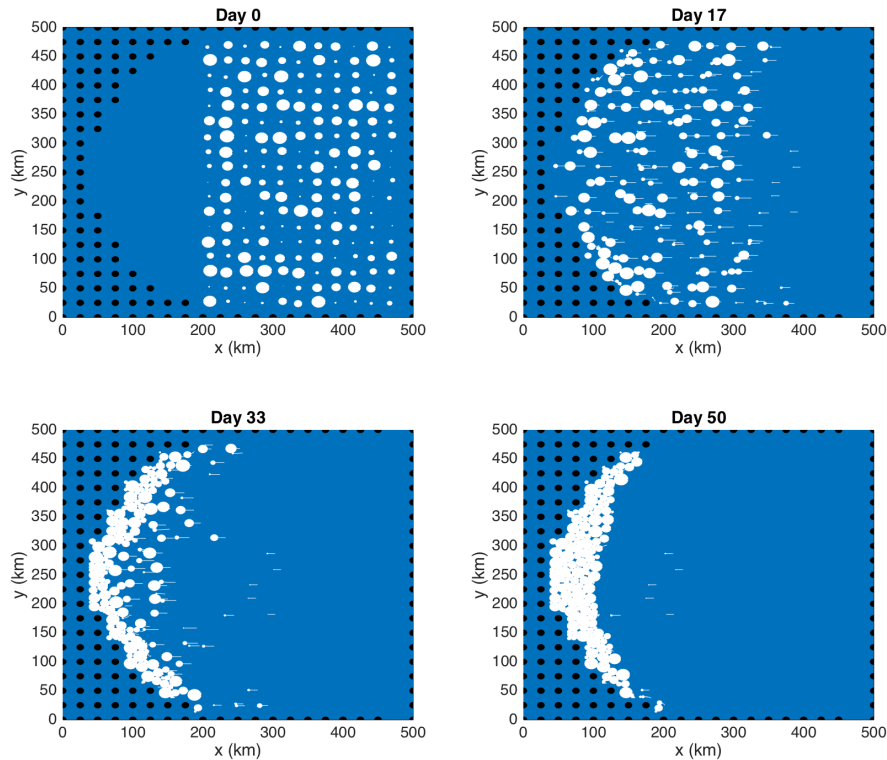
1058       **Figure 1.** Schematic showing how tabular icebergs are constructed using Lagrangian ele-  
 1059       ments. (a) Hierarchy of ice elements' physical structure: (i) Previous icebergs models represent  
 1060       icebergs using non-interacting point-particle elements; (ii) In the new framework ice elements are  
 1061       given finite extent so that they are able to interact with the ocean across multiple grid cells, and  
 1062       can interact with other elements; (iii) These finite extent elements can be joined together by nu-  
 1063       merical bonds (magenta lines) to form larger structures such as tabular icebergs. (b) Areal pho-  
 1064       tograph of a tabular iceberg with elements superimposed over it to illustrate how the Lagrangian  
 1065       elements can be used to model tabular icebergs. In this schematic the ice elements (purple dots)  
 1066       are initialized in a staggered lattice covering the surface area of the iceberg. For purposes of  
 1067       mass aggregation, the ice elements are assumed to have hexagonal shape (red hexagons). For  
 1068       purposes of element interactions, the ice elements are assumed to be circular (black circles).  
 1069       Elements are initially bonded to adjacent elements using numerical bonds (magenta lines). These  
 1070       numerical bonds form equilateral triangles which give the shape rigidity. An ocean grid has been  
 1071       included (dashed cyan lines). The background photo is an areal photograph of iceberg PIIB  
 1072       (Area= 42 km<sup>2</sup>) taken in Baffin Bay in 2012. A red ship can be identified on the bottom of the  
 1073       photo for scale.



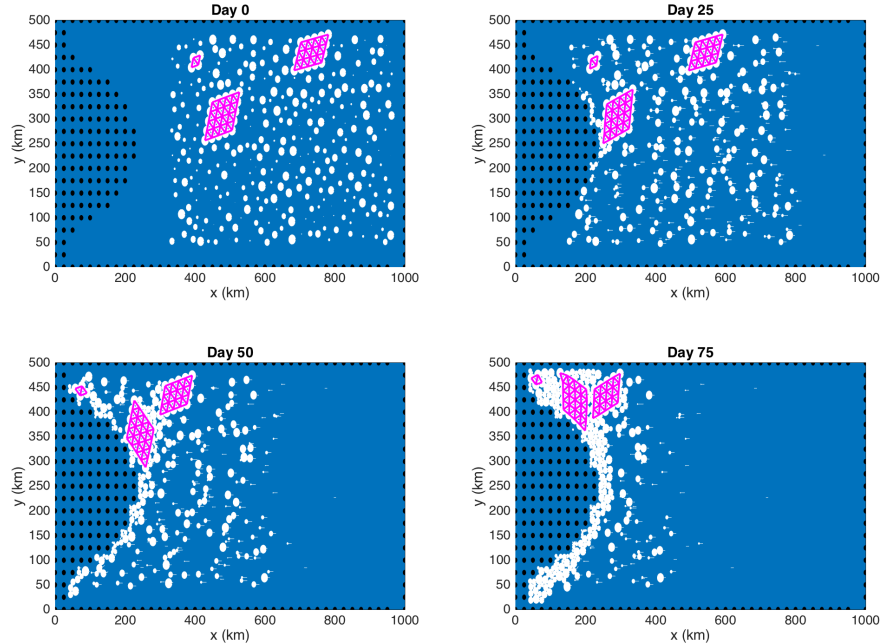
1074 **Figure 2.** Snapshots of the sea surface temperature in the tabular iceberg calving simulation.  
1075 Snapshots are taken (a) 7, (b) 15, and (c) 30 days after calving. Grid cells with ice mass  $\geq 10^4$  kg  
1076 are plotted in white, with grey shading indicating thinner ice. The dashed line in panel (c) shows  
1077 the location of the vertical transects shown in Figures 8 and 11.



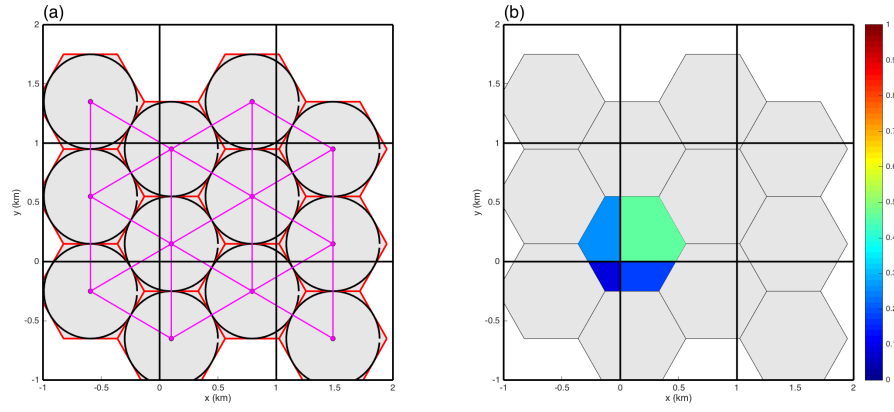
1078 **Figure 3.** Diagram showing the (a) repulsive and (b) attractive elastic interactive forces  
 1079 between two elements,  $i$  and  $j$ .  $R_i$  and  $R_j$  are the interactive radii of element  $i$  and  $j$ , respec-  
 1080 tively. The distance between the centers of elements is denoted as  $d_{ij}$ .  $L_{ij} = R_i + R_j$  is the  
 1081 critical-interaction-length scale.  $(F_e)_{ij}$  and  $(F_e)_{ji}$  are the elastic forces applied to elements  $i$  and  
 1082  $j$ , respectively (equation 7). A frictional damping force is also applied, which opposes the rela-  
 1083 tive velocity of the elements (not shown). The attractive forces are only applied when the two  
 1084 elements are bonded together (i.e.:  $B_{ij} = 1$ ).



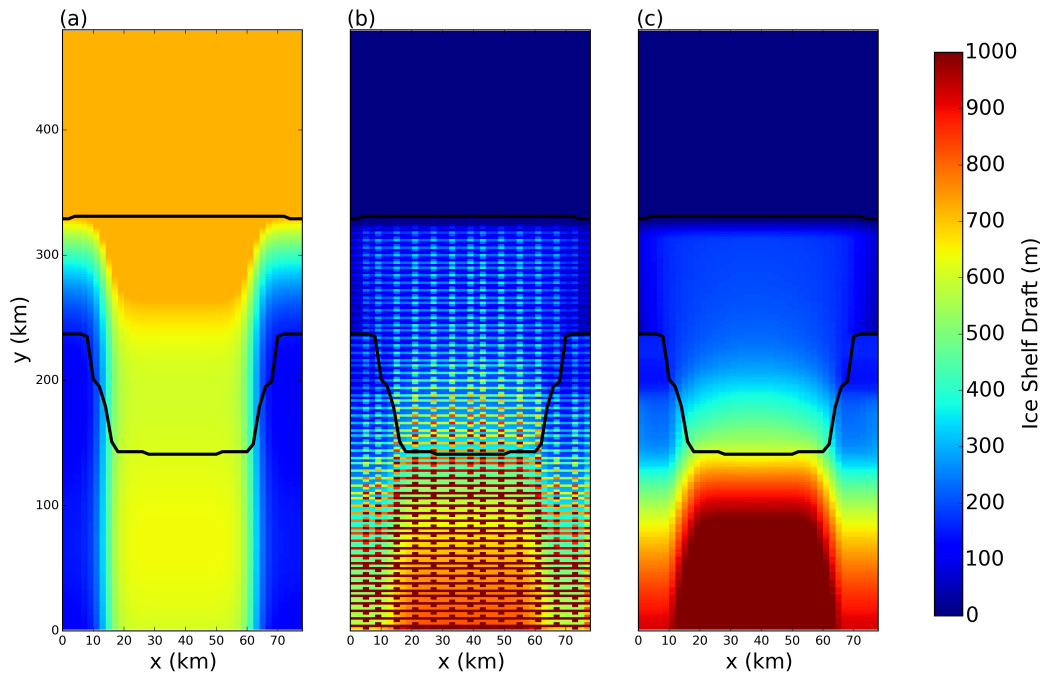
1085 **Figure 4.** Results of an uncoupled (ice-only) simulation with no bonds between ice elements.  
 1086 Ice elements are initialized throughout the domain, as shown in the top left panel. The elements  
 1087 are forced by an imposed westward ocean current of  $u=0.1\text{m/s}$  (no ocean model is used). Forces  
 1088 due to sea surface slope, atmospheric drag, Coriolis and sea-ice drag are set to zero. The figure  
 1089 shows snapshots of ice element positions at time  $t=0, 17, 33$  and  $50$  days. The size of the dots  
 1090 shows the surface area (and interaction radius) of each ice element. The white tails behind the  
 1091 elements show the elements' positions over the preceding two days. Land points are shown by  
 1092 black circles.



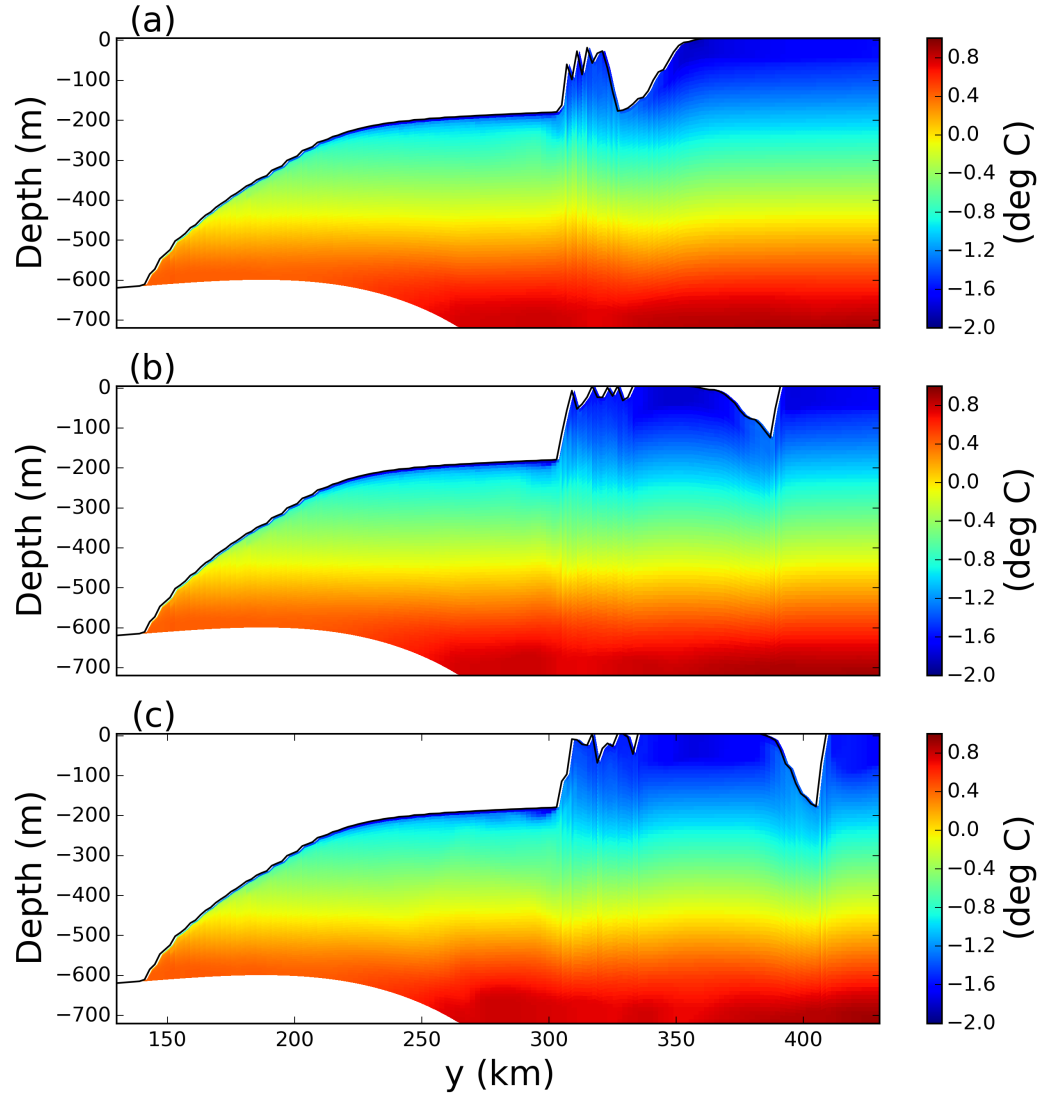
1093 **Figure 5.** Results of an uncoupled (ice-only) simulation using bonds between elements. Ice  
 1094 elements are initialized throughout the domain, as shown in the top left panel. Three tabular  
 1095 icebergs are included, with 25, 16 and 4 elements respectively. The elements are forced by an  
 1096 imposed westward ocean current of  $u=0.1\text{m/s}$  (no ocean model is used). Forces due to sea surface  
 1097 slope, atmospheric drag, Coriolis and sea-ice drag are set to zero. The figure shows snapshots  
 1098 of ice element positions at time  $t=0, 25, 52$ , and  $75$  days. The size of the dots shows the sur-  
 1099 face area (and interaction radius) of each ice element. The white tails behind the elements show  
 1100 the elements' positions over the preceding two days. Bonds between ice elements are plotted in  
 1101 magenta. Land points are shown by black circles.



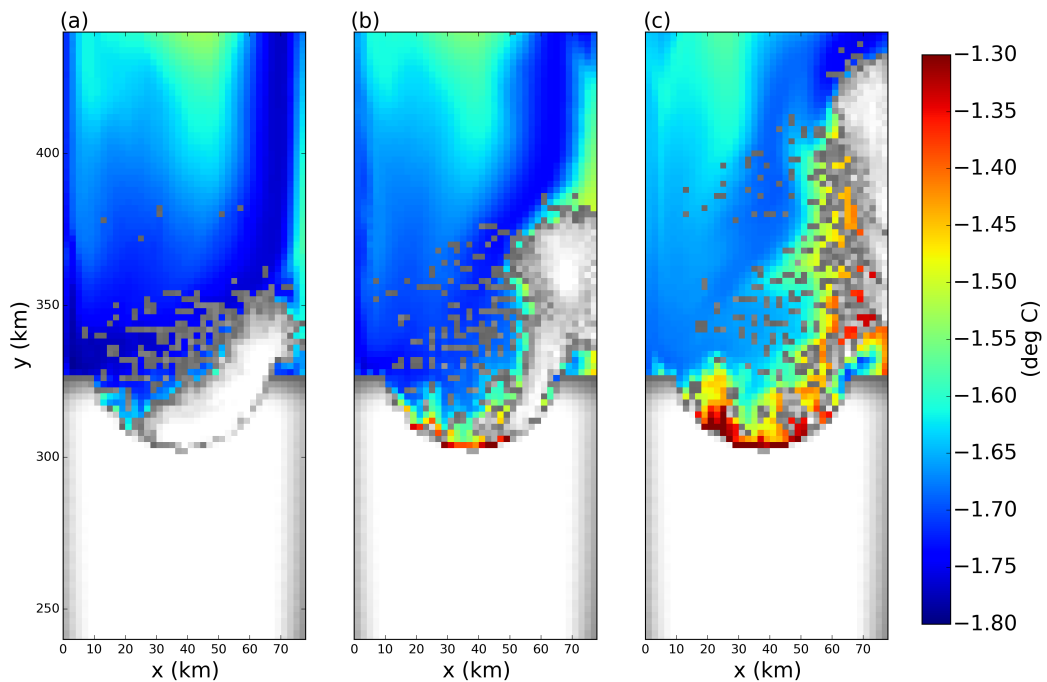
1102      **Figure 6.** (a) Ice element packing and geometry: ice elements (purple dots) are initialized  
 1103      in a staggered lattice. For purposes of mass aggregation, the ice elements are assumed to have  
 1104      hexagonal shape (red hexagons). For purposes of element interactions, the ice elements are  
 1105      assumed to be circular (black circles). Elements are initially bonded to adjacent elements us-  
 1106      ing numerical bonds (magenta lines). (b) Intersection of an hexagonal element and the ocean  
 1107      grid. The colors indicate the fraction of the hexagon that lies in each grid cell. These fractions  
 1108      are used as weights to spread the iceberg model properties to the ocean grid (see text for more  
 1109      details).



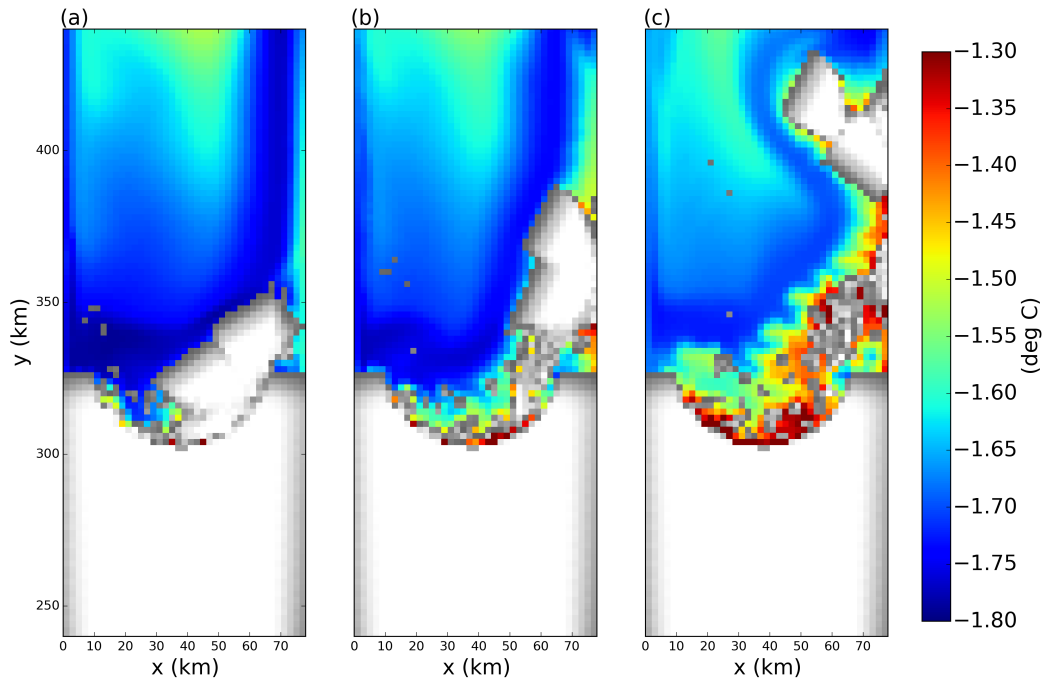
1110    **Figure 7.** (a) Ocean bottom topography and (c) ice-shelf draft used to initialized the tabular  
 1111    iceberg calving simulation. The ice draft is calculated from the total mass in an ocean grid  
 1112    cell after the mass-spreading interpolation has been applied (as explained in Section 2.3). Panel  
 1113    (b) shows the initial ice draft that would be calculated if the mass-spreading interpolation were  
 1114    not used (i.e. elements treated as point masses). The lower and upper black lines denote the  
 1115    grounding line and ice shelf front, respectively



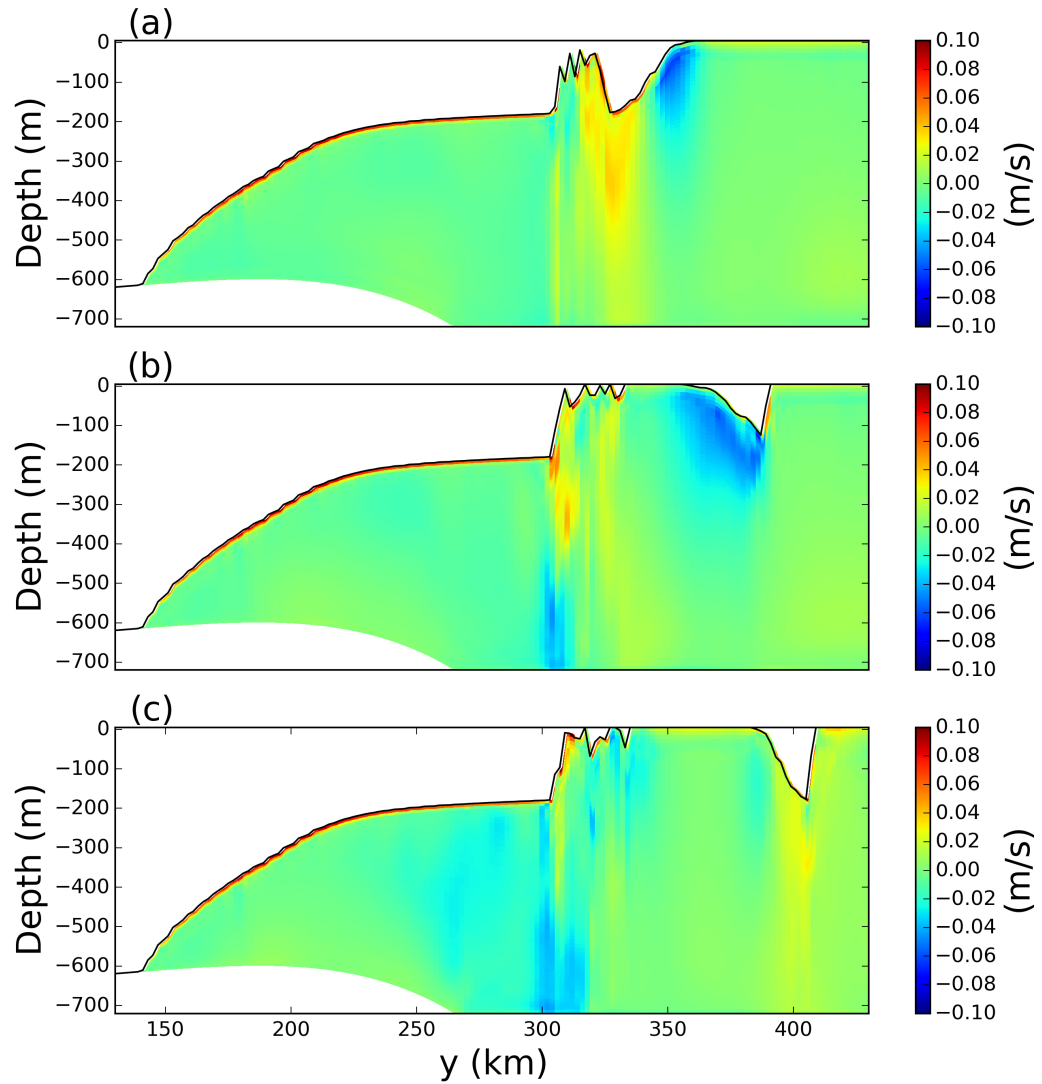
1116      **Figure 8.** Snapshots of vertical sections of ocean temperature at  $x = 54$  km in the tabular-  
1117      iceberg-calving Control experiment. Snapshots are taken (a) 7, (b) 15, and (c) 30 days after  
1118      calving. The position of the vertical transects is shown by the dashed lines in Figure 2c.



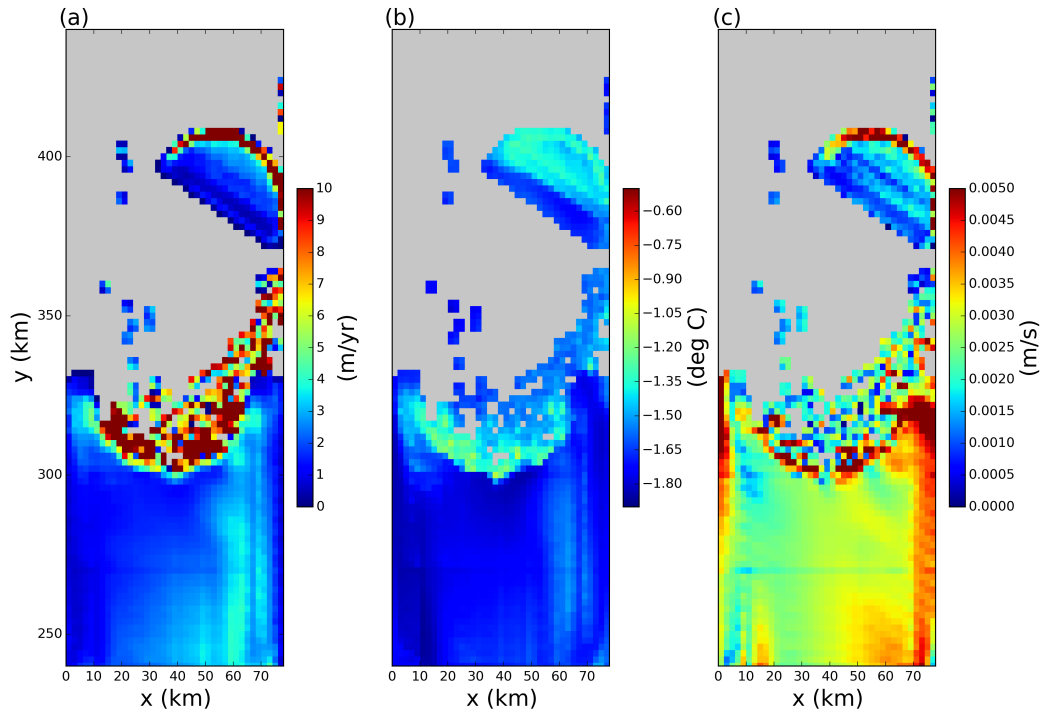
1119 **Figure 9.** No bonds simulation: Snapshots of the sea surface temperature for a simulation  
1120 where all bonds have been broken. Snapshots are taken (a) 7, (b) 15, and (c) 30 days after calv-  
1121 ing. Grid cells with ice mass  $\gtrsim 10^4$  kg are plotted in white, with grey shading indicating thinner  
1122 ice.



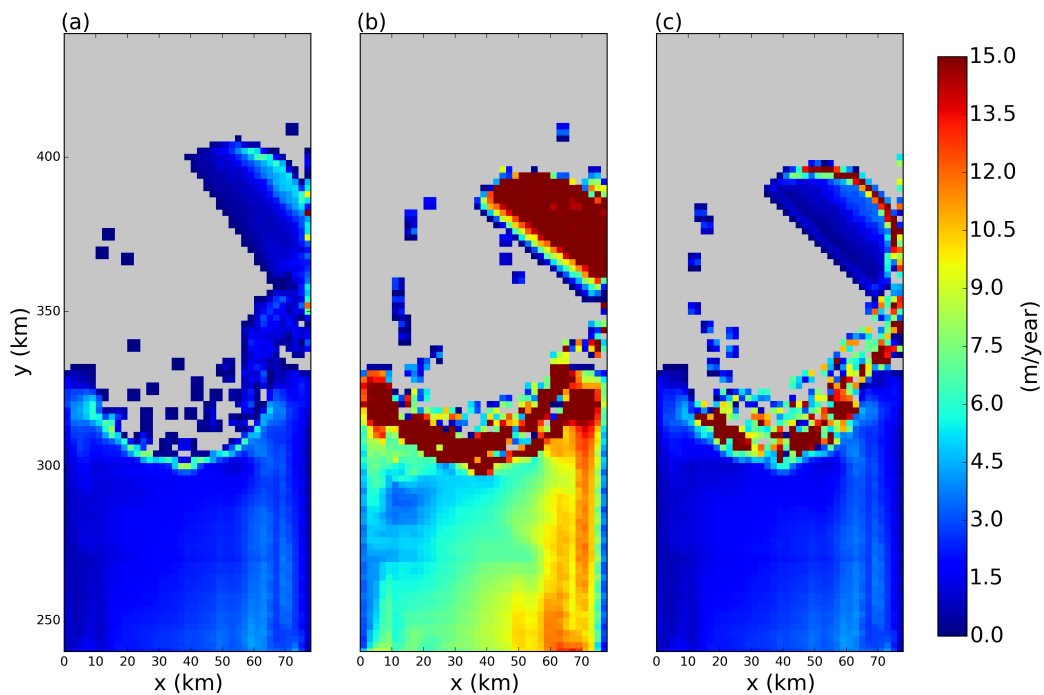
1123 **Figure 10.** Iceberg splitting simulation: Snapshots of the sea surface temperature for the ice-  
1124 berg splitting simulation. Snapshots are taken (a) 7, (b) 15, and (c) 30 days after calving. Grid  
1125 cells with ice mass  $\leq 10^4$  kg are plotted in white, with grey shading indicating thinner ice.



1126      **Figure 11.** Snapshots of vertical sections of meridional velocity at  $x=54$  km in the tabular-  
 1127      iceberg-calving Control experiment. Snapshots are taken (a) 7, (b) 15, and (c) 30 days after  
 1128      calving. The position of the transects is shown by the dashed line in Figure 2c.



1129 **Figure 12.** Results of the tabular-iceberg-calving experiment 30 days after the iceberg calves.  
1130 The three panels show snapshots of the (a) melt rate, (b) top-of-ocean temperature and (c) the  
1131 frictional velocity,  $u^*$ , at the base of the ice shelf. Ocean grid cells without ice are masked out in  
1132 grey.



1133 **Figure 13.** Results of three the tabular-iceberg-calving experiments using three different  
 1134 melt-rate parametrization. Panels show snapshots of the melt rate 30 days after calving for sim-  
 1135 ulations using the (a) three-equation-model melt-rate parametrization [Holland and Jenkins,  
 1136 1999], (b) icebergs-drift melt-rate parametrization point-particle-iceberg-melt parametrization  
 1137 [Gladstone et al, 2001], and (c) the mixed-melt-rate parametrization (introduced in as described  
 1138 in Section 2.5.). Ocean grid cells without ice are masked out in grey.